Application of Reconfigurable Field Perturbing Elements in Microwave Imaging within a Metallic Enclosure

by

Amir Hossein Ghasemi

A Thesis submitted to the Faculty of Graduate Studies of the University of Manitoba in partial fulfillment of the requirements for the degree of

Master of Science

Department of Electrical and Computer Engineering
University of Manitoba
Winnipeg, Manitoba, Canada

Abstract

One of the techniques to enhance the performance of microwave imaging (MWI) systems is to increase the amount of independent measured data that is collected when interrogating the object-of-interest (OI). A novel method is introduced which employs field perturbing elements (FPEs) to achieve this goal.

The research reported herein utilizes a cylindrical metallic enclosure having an octagonal cross-section, *i.e.* with flat-faceted walls on which a set of electrically controlled field perturbing elements (FPEs) that project into the chamber. The FPEs are implemented as printed circuit boards that include diodes that can be forward or reversed biased. Transmit and receive antennas are placed on the walls of the chamber and for each transmitter the interrogating field can be changed by turning one or more of the reconfigurable plates ON or OFF. This allows one to reduce the number of transmit antennas that are used. Our current system consists of an octogonally shaped chamber with four transmitter/receiver antennas. The size of the metallic chamber is on the order of a few wavelengths and with the entirety of the enclosure being made up of a conductive metallic material, it constitutes a quasi-resonant chamber (we utilize an open top adding some loss to the chamber).

The field perturbing elements include a pattern of segmented PCB traces with multiple diodes connecting the trace segments. To reduce the computational resources required to model these reconfigurable plates, the design criteria is to choose a pattern of the segmented PCB traces that minimally perturb the field within the chamber when the diodes are "OFF" (*i.e.* in reverse-biased mode) by choosing the frequencies that match closely with the numerical model. This allows us to remove the plates

from the numerical model when in the "OFF" mode with small effects on the accuracy. In the "ON" mode, the plates are modelled as PEC surfaces. To evaluate the performance of the proposed approach, a number of imaging experiments were performed with a DUT placed in two positions in the chamber for different configurations and combinations of the electrically reconfigurable plates. a comparison between two cases of FPE configurations have been performed. First, the case with FPEs in OFF mode and second, when the FPEs are in ON mode in two different frequencies. The critera for selecting the frequencies are also described. The results of the experiments are presented in this thesis.

Symbols and Acronyms

Symbol	Description
$\mathcal{S}$	Measurement domain
$\mathcal{D}$	Imaging domain
$\vec{E}^{tot}$	Total electric field
$\vec{E}^{inc}$	Incident electric field
$\vec{E}^{sct}$	Scattered electric field
$\vec{H}$	Magnetic fields
χ	Electric contrast of the object of interest
$\vec{\omega}$	Contrast source variable
$\vec{B}$	Magnetic flux density
$\vec{D}$	Electric flux density
ρ	Electric charge density
$\vec{\mathcal{M}}$	Imposed magnetic source
$\vec{\mathcal{J}}$	Imposed electric source
j	Imaginary unit: $\mathrm{j} = \sqrt{-1}$
ε_r	Relative complex permittivity of the object of interest
ε_b	Relative complex permittivity of the background
$\vec{r}$	Cartesian position vector
$\hat{x}$, $\hat{y}$, $\hat{z}$	Unit vectors along x, y and z directions
$\nabla\times$	Curl operator
$\nabla\cdot$	Divergence operator

Acronym	**Description**
MWI	Microwave imaging
MWT	Microwave tomography
FPE	Field perturbing element
OI	Object of interest
RI	Region of interest
USI	Ultrasonic imaging
TE	Transverse electric
TM	Transverse magnetic
MST	Modulated scattering technique
DST	Differential scattering technique
PEC	Perfect electric conductor
FEM	Finite element method
HDG	Hybridizable discontinuous galerkin
CSI	Contrast source inversion
PCB	Printed circuit board
SMD	Surface Mounted Diode
EIL	Electromagnetic Imaging Laboratory
E-field	Electric field
H-field	Magnetic field
EM	Electromagnetic
VNA	Vector network analyzer

Acknowledgments

First and foremost, I would like to thank my academic advisor, Dr. Joe LoVetri, for his direction and support during the course of my M.Sc studies.

I would also like to thank my colleagues Dr. Marzieh (Tamanna) Keleshteri, Kevin Brown, Max Houston, Amir Attar, Nicolas Geddert and Kyle Nemez. I would like to specially thank Dr. Mohammad Asefi for his guidance and encouragement during my program.

I would also like to express my appreciation for my M.Sc examiners: Dr. Puyan Mojabi and Dr. Dustin Isleifson for their efforts in the evaluation and examination of this work.

Finally, I extend my gratitude to MITACS and AGCO Corp for their financial support.

Contents

List of Figures

List of Tables

Chapter 1

Introduction

1.1 Microwave Imaging Overview

Recent developments in the field of Microwave Imaging (MWI) and its applications have led to renewed interest in further expansion of this field in various aspects. MWI is relatively low cost, portable, and is used in various applications from industrial non-destructive testing [1, 2] to uses in medical imaging. Microwave imaging is a category of general electromagnetic imaging where the utilized frequency band is normally in the range of 1GHz - 3GHz. Other applications of MWI include through-wall imaging [3], ground penetrating radars [4, 5], measurements of geophysical structures [6, 7] and grain bin imaging which has vast applications in the agriculture industry [8, 9, 10]. There is potential for various other applications where invasive methods are not feasible. MWI is particularly of significant import in the field of biomedical imaging such as breast cancer detection where non-invasive testing must be performed prior to any invasive testing [11, 12, 13, 14]. A general overview of different applications of biomedical imaging can be found in [15, 16, 17, 18].

There are two general types of MWI: qualitative and quantitative. In qualitative techniques, the reconstructed image of the target consists of different intensities without any corresponding values. Quantitative methods on the other hand, reconstruct a map of the region of interest (RI) by assigning specific permittivity values to each of the discretized elements in the regions. In this research, we work on obtaining a dielectric profile of an object of interest (OI) providing qualitative information regarding the shape and location of the OI, as well as some quantitative electromagnetic properties of those features [19], such as the permittivity profile of the OI which is the main objective of MWI.

A MWI system is normally comprised of an imaging chamber within which are installed a set of antennas typically one acting as a transmitter illuminating the RI and a set of receivers located at various positions within the chamber collecting the scattered field. For each illuminating field that is utilized to interrogate the OI, one collects data at several locations around the OI. The collected data over all the illuminating fields is the data that will be inverted to create an image of the complex-valued permittivity of the OI. Other hardware include a switching network to interface with the antennas, a vector network analyzer to send and receive microwave signals from the antennas. The measurements are in the form of S-parameters which are then converted into scattered field data through a calibration procedure, described in more details in chapter 5, that can be used to obtain quantitative information on the (RI) using inversion algorithms such as Finite-element contrast source inversion (FEM-CSI) [20]. Fig. 1 shows a general overview of a typical MWI system.

The common approach to increasing the amount of independent data is to increase the total number of transmitter/receiver pairs. However, the amount of data that can be collected using this common approach is limited by the resulting increase in the complexity of the system: there is a limited amount of space available around the OI to fix co-resident antennas. Even if a large number of antennas were to be used, space permitting, the required computational resources to include numerical models of the co-resident antennas within the inversion model would be too high. The proposed solution which is described in this work is to use FPEs to obtain/extract more information in a MWI system without adding more Tx/Rx pairs.

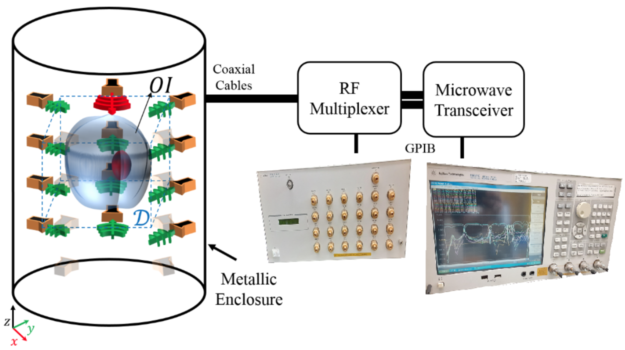

Figure 1: Overview of a typical Microwave Imaging System

1.2 Context on some of the Research Performed in the EIL

The Electromagnetic Imaging Laboratory (EIL)[21] at the University of Manitoba began its research with a focus on the use of ground-penetrating radar for landmine detection and has expanded into several different areas related to microwave imaging, ultrasonic imaging (USI)[22] and recently incorporating machine learning as a tool in performing MWI or USI or a combination of the two modalities [23]. The two main applications have been breast cancer imaging and the imaging of stored-grain for spoilage monitoring [24, 25, 26].

Antenna and probe design is a significant part of the imaging system. In [27], it is shown how a novel design of multiplexed Vivaldi antennas can be utilized to collect both transverse electric (TE) and transverse magnetic (TM) fields and in [28], it is described how a PCB based loop antennas can be utilized in a faceted quasi-resonant perfect electric conductor (PEC) chamber as magnetic field (H-Field) probes.

A crucial part of any imaging system besides hardware design such as antennas and the imaging chamber configuration, is the implementation of algorithms utilized to be able to invert the collected data and reconstruct the OI. In case of MWI the data is collected in the form of S-parameteres which is then converted to scattered electric or magnetic fields and is then used as input to, for example, the state of the art Contrast Source Inversion technique (CSI) which is a quantitative imaging technique utilizing full-wave, non-linear inversion technique. Another technique is the Gauss-Newton Inversion (GNI) [29]. In [30], Finite-element method is used as the discretization technique for the forward solver and CSI as inversion technique that reconstructs a permittivity map of the OI. This is referred to as the FEM-CSI technique. On the other hand, another discretization technique is developed at the EIL that follows the Hybridizable Discontinuous Galerkin (HDG) Method and CSI as Inversion technique (HDG-CSI) [31]. This method utilizes the same data as in FEM-CSI as input but uses the contrast in permeability, μ, of the object in addition to permittivity, ε. It inverts the collected fields on μ or ε that in turn creates a permeability or permittivity map of the OI. Multiplicative regularization (MR) can be used with any of the these methods, thus we have (MR-FEM-CSI, MR-DG-CSI, and MR-GNI). More details on general multiplicative regularization can be found in [32].

Besides MWI, a different modality of imaging has been developed that uses ultrasound. In USI, ultrasound pressure measurements are collected by piezo-electric transducers located within the ultrasound imaging chamber which is then fed to the algorithm described in [33] to reconstruct the ultrasound attenuation and speed map of the OI.

1.3 Motivation, Goals, and Scope

The accuracy and resolution of images produced using MWI depend heavily on the amount of independent data that can be collected through interrogating the OI by means of electromagnetic (EM) radiation. These data consist of EM fields measured at receiving antennas placed within the chamber. The EM field that is measured is the field that has been scattered from the target when illuminated by the field produced by a transmitting antenna.

One of the most crucial aspects for obtaining accurate reconstructions is the chamber design or more specifically its geometry. Chambers of circular-cylindrical shape have been consistently and productively used previously for MWI in the EIL. However, there are a number of potential disadvantages to using enclosures of this geometry such as modelling the chamber boundary using first-order tetrahedral elements. Utilizing an imaging chamber with flat facets means that we can more accurately model the fields at the boundaries compared with a cylindrical chamber. Due to the curvature of the boundary in a circular-cylindrical or a spherical chamber, using tetrahedral elements produces modelling error.

As indicated earlier, we have taken advantage of a metallic chamber. Touching upon some of the advantages of using a metallic enclosure, one can include the shielding effect that the conductive boundaries create from the outside noise, allowing better control and modelling of unwanted reflections and mutual coupling effects, giving rise to higher signal to noise ratio and quality factor. Additionally, a metallic chamber traps the electromagnetic energy inside the chamber that can lead to larger interrogating field strengths.

Since data are collected at the boundaries of the enclosure, only the normal component of the electric field and tangential components of the magnetic field are present. Therefore fewer measurements are required to characterize the fields at a given location. Furthermore, in this design a smaller chamber is developed compared to previous systems designed in the EIL.

To obtain a more accurate model of a system, either the complexity of the experimental system must be reduced, or the complexity of the model must be raised. The latter significantly adds to the computational burden while the former limits the choice of design of the MWI system including transceivers and the immersion media [34]. On the other hand, to obtain a high quality (better accuracy and resolution) image of the OI, a MWI system is to be designed in a manner that as much non-redundant data can be collected as possible.

Traditionally, the common methods to achieve this goal have been to use multiple frequencies or using a higher number of transmitters and receivers [35], or making use of a rotational enclosure to break the symmetry and introduce more unique information in the collected fields [36] to expand the total amount of collected data. Using mechanical/rotational boundaries as well as increasing the number of Tx-Rx pairs add to the complexity and design of the system. Imaging in highly resonant enclosures can be highly frequency dependent and imaging at different frequency points can drastically change the outcome of the inversions. This points out the necessity to have a frequency selection procedure details of which are discussed in chapter 5.

The novel method that is introduced in this thesis expands upon the utilization of field perturbing elements (FPEs) to increase the amount of non-redundant data while using a low number of sources and receivers in the chamber and collecting data at a single frequency [37].

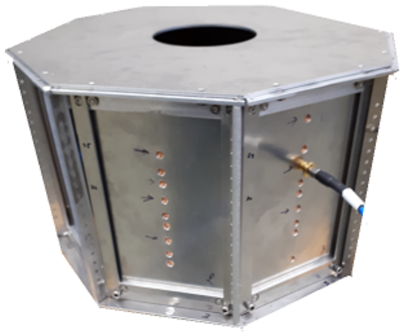

Figure 2: Novel Metallic Octagonal Chamber

For this set up, the novel metallic octagonal chamber that was designed is shown in Fig. 2. Four co-resident antennas are set up on the walls of the octagonal chamber with one on four of the eight sides. At any one data collection cycle, one antenna is transmitting and the other three act as receivers. The FPEs will be toggled between ON/OFF modes during each of the data collection cycles creating more non-redundant fields which leads to higher amount of independent data.

1.4 Thesis Outline

Chapter 2 provides an overview on the theoretical background of MWI as well as some of the previous work done to achieve a higher amount of useful data in our MWI system.

Chapter 3 puts the emphasis on the design of the system and setting up of the experiments to validate the new technique. Utilization and operation of the vector network analyzer (VNA) as well as the probe driver is discussed as well as the operation and design of the field pertubing elements (FPEs).

In Chapter 4, a numerical study is conducted to examine the feasibility of the design and to validate the performance of the FPEs as well as the ability to enhance the final image in a synthetic framework.

In Chapter 5, the experimental results as well as the calibration techniques utilized are studied and analyzed. As pointed out earlier, the performance of the FPE technique and its effectiveness in the outcome of the inversions, is highly frequency dependent due to using a highly resonant chamber, as will be shown, and therefore a frequency selection procedure is required. A detailed description on selecting proper frequencies is provided in this chapter. Monopole antennas are utilized as transmitter/receiver and electric field data are collected in the experimental process.

In Chapter 6, we provide a summary of the work presented in this thesis and describe briefly that in a MWI system, when the amount of non-redundant data is increased using the FPEs, the resulting image reconstruction is significantly improved. Additionally, an outline of some of the possible future work is also provided that one might build upon and follow.

Chapter 2

Theoretical Background and Literature Review

2.1 Theoretical Background of Microwave Imaging

The goal of a MWI problem is to reconstruct the constitutive parameters of an object of interest (OI) that is located in the imaging domain $\mathcal{D}$. The constitutive parameters of interest are the complex-valued permittivity ε and permeability μ. This is done by illuminating the imaging domain with microwaves propagated from transmitters placed in the measurement domain $\mathcal{S}$ and collecting the scattered electromagnetic fields.

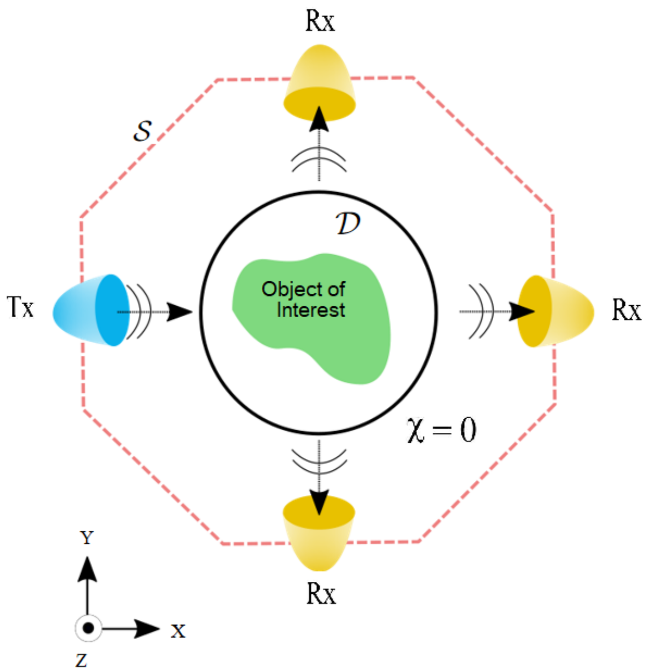

Figure 3: Geometrical schematic of the microwave imaging system. Tx and Rx represent the transmitting and receiving antennas respectively. The domain $\mathcal{D}$, which contains the "object of interest", is the imaging domain. The domain $\mathcal{S}$ contains the transmitting and receiving antennas

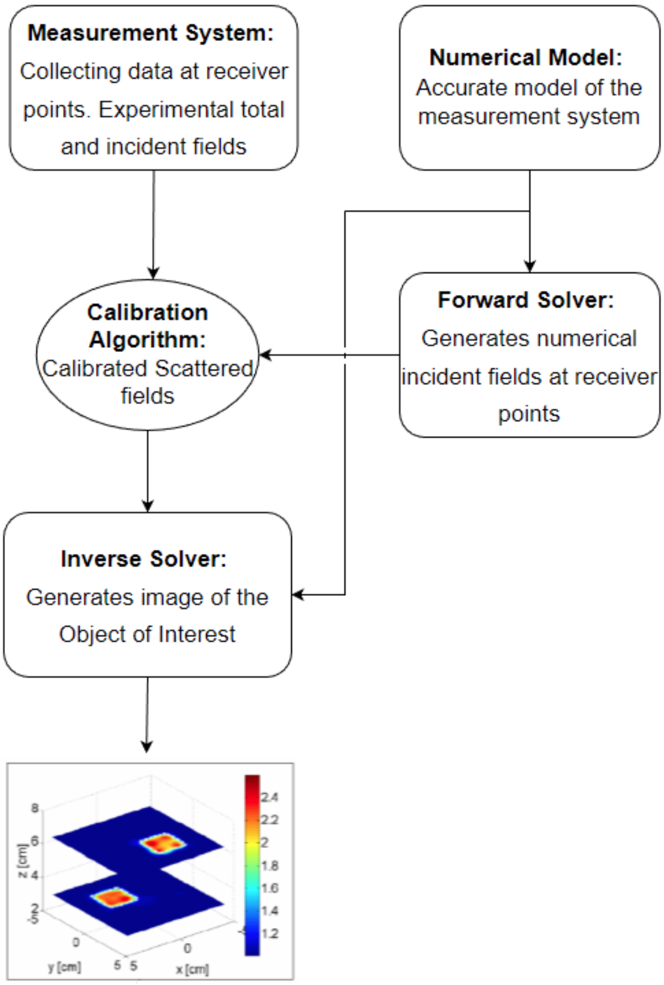

Figure 4: An overview of MWI procedure

These measured fields are the source of information in finding the constitutive parameters of the OI. The scattered fields are defined as:

$$E^{sct}(\vec{r}) \triangleq E(\vec{r}) - E^{inc}(\vec{r}) \tag{1}$$

where $E(\vec{r})$ and $E^{inc}(\vec{r})$ are electric fields in the presence of the OI and in absence of it at position $\vec{r} = (x, y, z)$, respectively.

In a MWI system, an accurate numerical model of the experimental measurement setup includes the numerical background and transmitter and receiver probes (EM data sources and collectors). A "Forward" Solver is employed to collect numerical data based on the synthetic model of the system. These data are used in conjunction with the experimentally measured data and are input into an "Inverse" Solver, to reconstruct an image of the OI. Fig. 4 provides an overview of this procedure. The inverse solver used in this work is the FEM-CSI developed at the EIL [30]. It considers the inverse problem as an optimization problem and minimizes the difference between the actual measured fields and those generated by the forward solver.

In what follows, we describe how the scattered field is formulated based on the total and incident fields, as well as obtaining the field equation that is iteratively solved by the FEM-CSI solver to ultimately reconstruct the complex permittivity of the object of interest. The total and incident fields satisfy the Maxwell's equations in differential form. These are in the frequency domain assuming e^{jwt} time dependency:

$$\nabla \times \vec{E} = -j\omega\vec{B}(\vec{r}) + \vec{\mathcal{M}}(\vec{r}) \tag{2}$$

$$\nabla \times \vec{H} = j\omega\vec{D}(\vec{r}) + \vec{\mathcal{J}}(\vec{r}) \tag{3}$$

$$\nabla \cdot \vec{D}(\vec{r}) = \rho(\vec{r}) \tag{4}$$

$$\nabla \cdot \vec{B}(\vec{r}) = 0 \tag{5}$$

Here, $\vec{D}(\vec{r})$ is the electric flux density, $\rho(\vec{r})$ is the electric charge density, $\vec{B}(\vec{r})$ is the magnetic flux density, $\vec{E}(\vec{r})$ and $\vec{H}(\vec{r})$ are the total electric and magnetic fields, j is the imaginary unit equal to $\sqrt{-1}$, ω is the angular frequency equal to $2\pi f$ and $\vec{\mathcal{M}}(\vec{r})$

and $\vec{\mathcal{J}}(\vec{r})$ are imposed magnetic and electric sources, respectively.

Taking into account the constitutive relationships $\vec{D}(\vec{r}) = \varepsilon(\vec{r})\vec{E}(\vec{r})$ and $\vec{B}(\vec{r}) = \mu(\vec{r})\vec{H}(\vec{r})$ and substituting them into (2) and (3) and considering the OI to be non-magnetic and assuming no magnetic sources we get:

$$\nabla \times \vec{H}(\vec{r}) = j\omega\varepsilon(\vec{r})\vec{E}(\vec{r}) + \vec{\mathcal{J}}(\vec{r}) \tag{6}$$

$$\nabla \times \vec{E}(\vec{r}) = -j\omega\mu_o\vec{H}(\vec{r}) \tag{7}$$

Where $\varepsilon(\vec{r}) = \varepsilon_o\varepsilon_r(\vec{r})$ is the complex permittivity and μ_o is the free space permeability. In our work, the object is assumed to be non-magnetic and thus, μ_r is considered to be one. The complex permittivity ε at position $\vec{r}$ is:

$$\varepsilon(\vec{r}) = \varepsilon'(\vec{r}) - j\varepsilon''(\vec{r}) \tag{8}$$

Taking curl of Eq. 7 we will have:

$$\nabla \times \nabla \times \vec{E}(\vec{r}) = -j\omega\mu_o\nabla \times \vec{H}(\vec{r}) = \omega^2\mu_o\varepsilon(\vec{r})\vec{E}(\vec{r}) - j\omega\mu_o\vec{\mathcal{J}}(\vec{r}) \tag{9}$$

Here, the wave-number k is defined as:

$$k^2(\vec{r}) = \omega^2\mu_o\varepsilon(\vec{r})\varepsilon_o \tag{10}$$

Substituting Eq. 10 into Eq. 9 we get:

$$\nabla \times \nabla \times \vec{E}(\vec{r}) - k^2(\vec{r})\vec{E}(\vec{r}) = -j\omega\mu_o\vec{\mathcal{J}}(\vec{r}) \tag{11}$$

Similar formulation can be written for the electric incident field $\vec{E}^{inc}(\vec{r})$ that is defined as the field produced by the sources in the background (absence of OI).

$$\nabla \times \nabla \times \vec{E}^{inc}(\vec{r}) - {k_o}^2(\vec{r})\vec{E^{inc}}(\vec{r}) = -j\omega\mu_o\vec{\mathcal{J}}(\vec{r}) \tag{12}$$

Here, the background wave-number can be written as $k_o^2 = \omega^2\mu_o\varepsilon_o$.

Based on formula described in (1), by subtracting Eq. 12 from Eq. 11, scattered field will be obtained:

$$\nabla \times \nabla \times (\vec{E}(\vec{r}) - \vec{E}^{inc}(\vec{r})) - k^2(\vec{r})\vec{E}(\vec{r}) + {k_o}^2\vec{E^{inc}}(\vec{r}) = 0 \tag{13}$$

Rewriting the above equation in terms of scattered fields, we get:

$$\nabla \times \nabla \times \vec{E}^{sct}(\vec{r}) - {k_o}^2\vec{E}^{sct}(\vec{r}) = (k^2(\vec{r}) - {k_o}^2)\vec{E}(\vec{r}) \tag{14}$$

When electromagnetic fields illuminate an object, the scattered field can be represented as being produced by contrast sources, $(k^2 - {k_o}^2)\vec{E}(\vec{r})$, as in the right-hand-side of Eq. 14. The contrast source $w(\vec{r})$ is the induced current in the object created by the incident field and is defined per transmitter as:

$$\vec{w}(\vec{r}) \triangleq \chi(\vec{r})\vec{E}(\vec{r}) \tag{15}$$

Here, $\chi(\vec{r})$ is the dielectric contrast that is satisfies the following relation:

$$\chi(\vec{r}) = \frac{\varepsilon_r(\vec{r}) - \varepsilon_o}{\varepsilon_o} \tag{16}$$

Based on the above formulations, we will obtain the scattered field for a transmitter t, that is governed by the vector wave equation inside the imaging domain $\mathcal{D}$ as follow:

$$\nabla \times \nabla \times \vec{E_t}^{sct}(\vec{r}) - {k_o}^2 \vec{E_t}^{sct}(\vec{r}) = {k_o}^2 \vec{w}_t(\vec{r}) \tag{17}$$

The vectorial partial differential Eq. (17) can be solved using FEM given a set of boundary conditions details of which are given in [38].

In the Dynamic Boundary Model Contrast Source Inversion (DMCSI) which is a generalization of (CSI) algorithm, boundary conditions of the finite element model are no longer assumed to be fixed; By changing boundaries we get varying total fields which are the illuminating fields that induce contrast sources. Although there will be a different contrast source for each boundary condition that is incorporated, the contrast will remain the same. DMCSI works to update the contrast, χ, and contrast sources, w, iteratively to ultimately minimize the cost functional within the framework of the finite-element method. The DMCSI cost functional is made up of two functionals:

$$\mathcal{F}^{DMCSI}(\underline{\chi}, \underline{\vec{\omega}_\tau}) = \mathcal{F}^{\mathcal{D}}(\underline{\chi}, \underline{\vec{\omega}_\tau}) + \mathcal{F}^{\mathcal{S}}(\underline{\vec{\omega}_\tau}) \tag{18}$$

Where $\underline{\vec{\omega}_\tau}$ is the contrast source vector per changing transmitter τ or changing boundary conditions (BCs). The normalized data-error $\mathcal{F}^{\mathcal{S}}(\underline{\vec{\omega}})$ and the normalized domain-error $\mathcal{F}^{\mathcal{D}}(\underline{\chi}, \underline{\vec{\omega}})$ are given by:

$$\mathcal{F}^{\mathcal{S}}(\underline{\vec{\omega}_\tau}) = \frac{\sum_\tau \left\| \underline{\vec{E}}_\tau^{sct,meas} - \vec{\mathcal{M}}_{\mathcal{S}} \vec{\mathcal{L}}_\tau [\underline{\vec{\omega}_\tau}] \right\|_{\mathcal{S}}^2}{\sum_\tau \left\| \underline{\vec{E}}_\tau^{sct,meas} \right\|_{\mathcal{S}}^2} \tag{19}$$

$$\mathcal{F}^{\mathcal{D}}(\underline{\chi}, \underline{\vec{\omega}_\tau}) = \frac{\sum_\tau \left\| \underline{\chi} \odot \underline{\vec{E}}_\tau^{inc} - \underline{\vec{\omega}_\tau} + \underline{\chi} \odot \vec{\mathcal{M}}_{\mathcal{D}} \vec{\mathcal{L}}_\tau [\underline{\vec{\omega}_\tau}] \right\|_{\mathcal{D}}^2}{\sum_\tau \left\| \underline{\chi} \odot \underline{\vec{E}}_\tau^{inc} \right\|_{\mathcal{D}}^2} \tag{20}$$

Here, τ denotes changing the transmitters and/or changing BCs in the finite element model, $\mathcal{M}_{\mathcal{S}}$ and $\mathcal{M}_{\mathcal{D}}$ are interpolatory matrix operators, $\vec{\mathcal{L}}_\tau$ is the inverse FEM operator that incorporates the boundary conditions, $\underline{\vec{E}}_\tau^{sct,meas}$ is a vector of the measured scattered fields at receiver locations per transmitter and or BCs in $\mathcal{S}$, $\underline{\vec{E}}_\tau^{inc}$ contains the incident field values in $\mathcal{D}$ and $\underline{\chi}$ is the contrast values located in $\mathcal{D}$. Details on the above FEM-CSI formulation are provided in [30, 35, 39, 40]. A description of the MR regularization techniques applied to the inversion is provided in [41] and [42].

2.2 Significance of the Amount of Independant Interogration Fields

When designing microwave imaging (MWI) systems, it is important to consider the amount of independent data that can be collected by the system. The number of independent measurements can be increased by using arbitrarily positioned antennas in a non-symmetric imaging chamber. However, the total number of antennas in an imaging system is limited by the size of the chamber, switching mechanism such as the one shown in Fig. 5, including the hardware to feed the antennas as well as mutual coupling between the antennas.

Figure 5: RF switch device used in order to multiplex the VNA ports and feed the 24 port systems

It has been well established that in any microwave imaging system, the accuracy of the reconstructed permittivity map of the OI is proportional to the amount of scattered field data collected at the receiver points within the chamber. That is, the higher the amount of independent data collected, the more accurate the reconstructed permittivity of the target will be [43, 44].

There are several published studies that have attempted to expand the amount of non-redundant data with focus on chamber design to improve the overall performance and versatility of a microwave imaging system [45], as well as the ways in which the interrogating fields can be varying either by changing the boundaries [36] or by introducing external elements within the chamber such as FPEs to manipulate the electromagnetic fields [39]. Fig. 6 shows the chamber used in [39].

There are two fundamental techniques which provide one the ability to increase the total amount of data to be collected. First, by increasing the total number of spatial sampling points and second, by increasing the amount of non-redundant interrogating fields. Normally, increasing the spatial sampling points requires more resources in the form of more probes which in turn requires a switching mechanism hardware leading to an increased cost and complexity of the design. For instance [34] has used 24 co-resident probes at 24 different receiver points within the chamber utilizing a 24-port switch to feed the system.

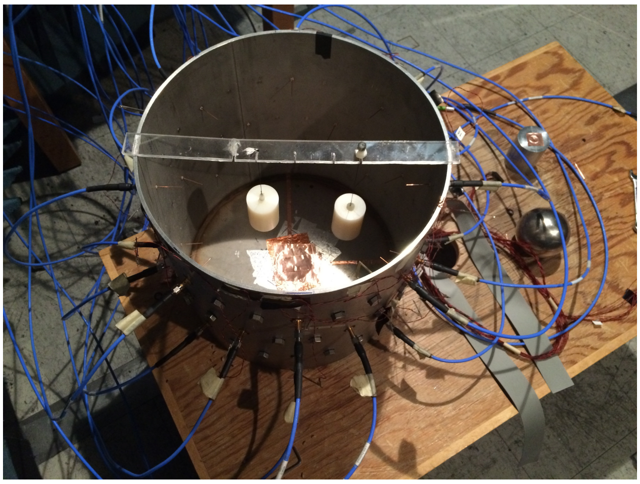

Figure 6: Cylindrical chamber with 24 monopole antennas used in [39]

It is shown in [27], how a novel design of multiplexed Vivaldi antennas can be utilized to collect both transverse electric (TE) and transverse magnetic (TM) by placing the probes in horizontal and vertical positions inside the chamber thus collecting more polarizations of the field in order to increase the amount of data. The Vivaldi antenna used is shown in Fig. 7.

Although increasing the number of probes especially within a PEC chamber has the added draw back of mutual coupling effects which can have considerable effects on the system performance as well as additional devices which ultimately leads to a more complex and expensive MWI system.

Figure 7: one of the Vivaldi antennas used in [27]

Techniques such as the modulated scattering technique (MST) [46] or the differential scattering technique (DST) [19] have been developed to increase the number of spatial sampling points without the need to increase the number of receiver points as well as avoiding some of the problems associated with mutual coupling of the antennas. However, MST/DST probes can only be used to increase the number of spatial sampling points and not the amount of interrogating fields. This limitation can have a significant effect on the accuracy of the image reconstructed from these field data [47].

On the other hand, the techniques considered herein leading to the generation of unique illuminating fields and thereby eliminate several of these drawbacks by allowing us to use fewer antennas which lead to less mutual coupling effects as well as eliminating the need for an additional switching device to feed a high number of probes. In [39], it has been shown how increasing the amount of interrogating fields by making use of active elements placed within the chamber can help enhance the reconstructed permittivity map of a dielectric target inside a metallic chamber.

Also in [36], it has been shown how a rotatable conductive enclosure is used to increase the amount of interrogating fields that are collected at each static position of the chamber by making use of a minimal antenna array having as few as only four co-resident antennas. The antenna array remains fixed with respect to the imaging domain and only the boundary of the PEC chamber is rotated leading to creation of more non-redundant field data without the need to add more probes to create higher spatial sampling points.

In the research presented herein we show that using a small active field perturbing element inside a conducting imaging chamber can enhance the imaging performance by removing the symmetry of the field distribution and increasing the number of illuminating fields [39]. We investigate the effect of using dynamic boundaries for changing the distribution of the fields inside a chamber. We investigate their effect on increasing the amount of independent interrogating fields. Numerical and experimental results from a simple wooden target in air background will be used to show the effectiveness of this technique.

Chapter 3

Hardware Setup and Implementation

3.1 Field Perturbing Elements

In metallic enclosures, the placement of conducting objects can considerably vary the field distribution within the chamber. As will be shown, increasing the number of illuminating sources by including Field Perturbing Elements (FPEs) to the imaging system has a significant effect on the enhancement of the reconstruction results. FPEs influence the performance of a microwavce imaging system by perturbing the interrogating fields within the chamber leading to a higher amount of non-redundant data.

The chamber consists of eight sides that are screwed together and the open space between each side is covered by copper tape to ensure proper shielding. The reconfigurable plates are placed in between the adjacent sides held firmly by bolts from outside the chamber. The placement of the FPEs within the chamber is depicted in Fig. 8 and Fig. 9. Two of the monopole antennas are also shown in the figure.

There are two FPEs placed in the chamber across from eachother at different depths from the top of the chamber. The placement of the monopole E-field probes as well as the FPEs are visible in the figures below.

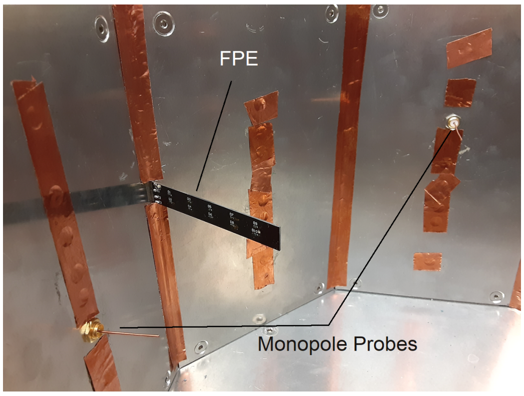

Figure 8: Placement of FPEs within the PEC Octagonal Chamber

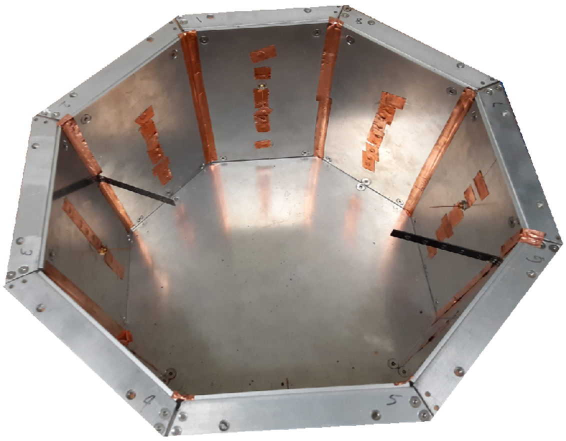

Figure 9: Placement of FPEs within the PEC Octagonal Chamber (perspective view)

Each FPE printed circuit board (PCB) is comprised of five conducting traces (segments). There are diodes on each segment and the length of each segment is 1 cm and with spacing of 1.8 mm between every two segments as shown in Fig. 10. They are implemented on a printed circuit board which are controllable in the sense that they can be put to forward or reversed biased mode. With the microwave frequency of operation being 1GHz - 2GHz, when in forward biased mode (ON), the traces will be electrically connected to create a long shorting element that will perturb the electromagnetic waves within the chamber. When in reversed biased mode (OFF), the traces are effectively broken into small 1 cm segments that are effectively invisible to the waves inside the chamber. Figure below shows the Field perturbing element:

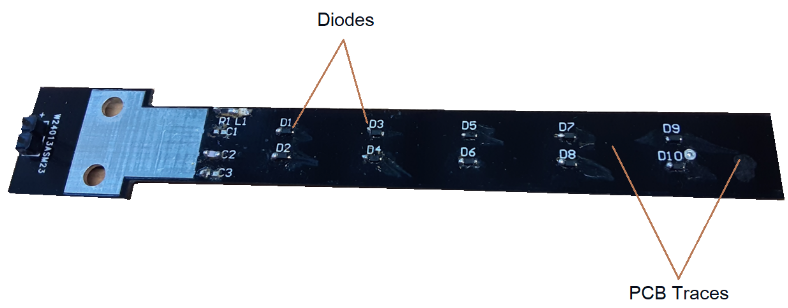

Figure 10: Field Perturbing Element

The electronic design of the FPEs was implemented on a PCB using surface mount SMD parts including resistors, capacitors and diodes. An input voltage of 6.5V - 10V is used at the D.C. input terminals of the FPE to control the bias of the diodes. The input DC voltage is controlled using the driver circuit device that reads commands directly from the accompanying computer to control which FPE should be put in ON/OFF mode at any one time. Fig. 11 shows the electronic schematic of the FPE.

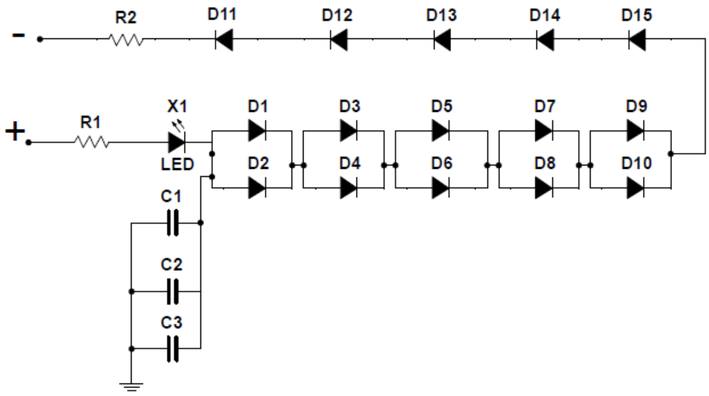

Figure 11: schematic of the Field Perturbing Element

For more clarification on how each FPE trace is integrated in the design, the following figure shows the utilization of diodes to connect the traces together and to have the ability to connecting and disconnecting them using a command computer. The three bypass capacitors are implemented to prevent short circuit and to ensure the diodes will be forward biased when voltage is applied at the input. The negative terminal is grounded in the power source.

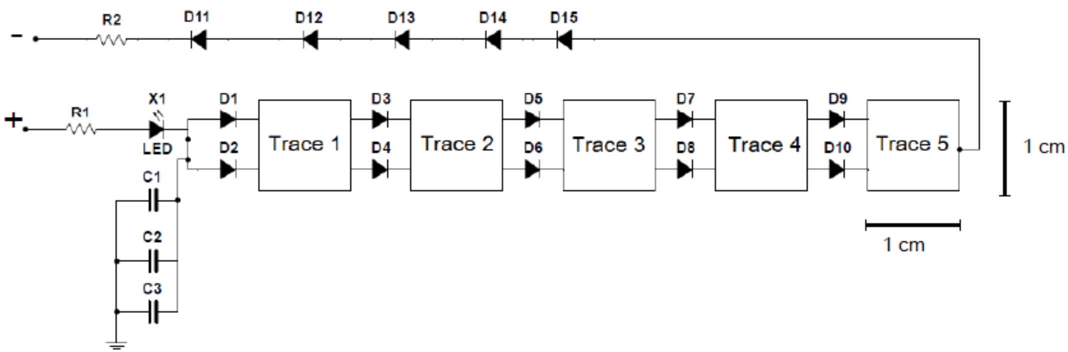

Figure 12: Integration of the sub-wavelength traces in the PCB design

Fig. 13 and Fig. 14 show the high frequency equivalent circuit of the FPEs in OFF and ON modes as seen by the illuminating wave.

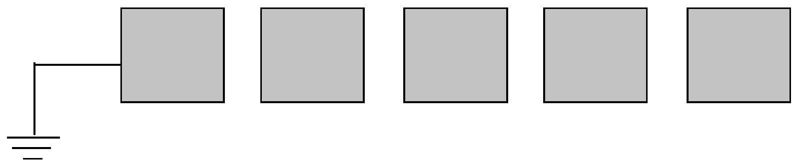

Figure 13: High frequency model for the Field Perturbing Element in OFF mode

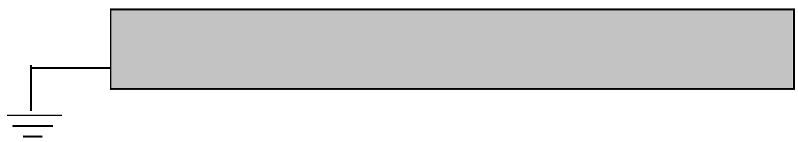

Figure 14: High frequency model for the Field Perturbing Element in ON mode

Values of the parts are shown below:

- R_1 = 110 Ohms
- R_2 = 110 Ohms
- C_1 = 215 PF
- C_2 = 210 PF
- C_3 = 210 PF

The part number for the surface mount PIN diodes are BAR64-02V. The voltage drop across each of the diodes in an unbiased state is 0.648 V and the voltage drop across the LED is 1.7 V. To put the diodes in forward or reversed biased mode, the FPEs are connected to the proper end (positive or negative) of the probe driver details of which are described in section 3.3. In forward biased state, the five patches (traces) shown in Fig. 12 will be electrically shorted, at microwave frequencies, forming a long PEC plate which in turn will perturb the fields.

On the other hand, when in reversed biased or in OFF mode, each of the five patches shown in the figure will be disconnected from one another leading to a series of short segments that, at microwave frequencies, will be invisible to the fields within the chamber as the length of the individual elements will be much less than that of the wavelength $l << \lambda$.

3.2 Chamber Design

Throughout this work, we take advantage of of the electrically conductive sides of our imaging chamber which serves as both probe and FPE holder (on the inside of the walls) as well as a shield from outside interference. Utilizing a quasi-resonant chamber of this type significantly varies the distribution of the electromagnetic energy in comparison with that of an open system. The field distribution is now in the form of standing-wave modes. These will be quite complicated because of the octagonal shape of the chamber and the open top. Making use of PEC boundaries of the chamber allows for more accurate modelling of reflections at the boundary because the PEC boundaries can be easily modelled using PEC boundary conditions on the tetrahedral facets in the FEM code.

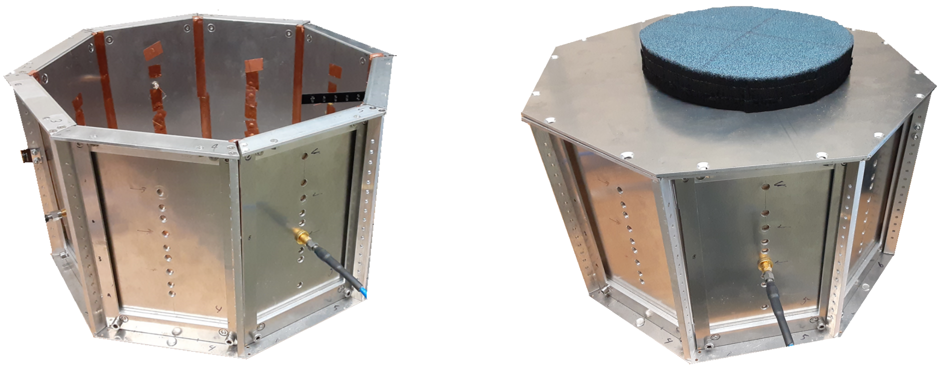

(a) Octagonal Metallic Enclosure with Open Top **(b)** Octagonal Metallic Enclosure in Imaging Mode

Figure 15: Metallic Octagonal Chamber used in this Experiment

Fig. 15 shows the constructed measurement chamber. Each of the four thin wire monopole E-field antennas are attached to one of the side walls positioned across from one another. Two of the probes are located 11 cm from the top surface of the chamber and two of them located 7 cm from the top surface to create a more asymmetrical setting. The two FPEs are also placed across from each other on different depths from the top surface at 3.7 cm and 7.6 cm respectively. The schematic depiction of the chamber including the probes and the FPEs are shown in Fig. 16 and Fig. 17.

The design of this quasi-resonant chamber allows data collection for both H-field as well as E-field. Collection of each of these field components require a different type of antenna. Also, as a robust design, the chamber allows for an arbitrary number of probes to be placed in it. To this end, there are holes drilled on each wall to place the antennas and the extra drill holes are covered by copper tape for shielding purposes for scenarios where a small number of antennas are being utilized.

In Fig. 16 and Fig. 17, the antenna positions within the octagonal chamber are marked by blue dots and the electric field polarization each antenna receives is shown by red arrows, i.e., each antenna is sensitive to the normal electric field E_n polarization. Each probe's polarization is relative to the facet it is adhered to. *i.e.* each E_n probe measures the component of the electric field that is normal to its facet. The FPE plates are also shown in the figures below and their positions within the enclosure is specified.

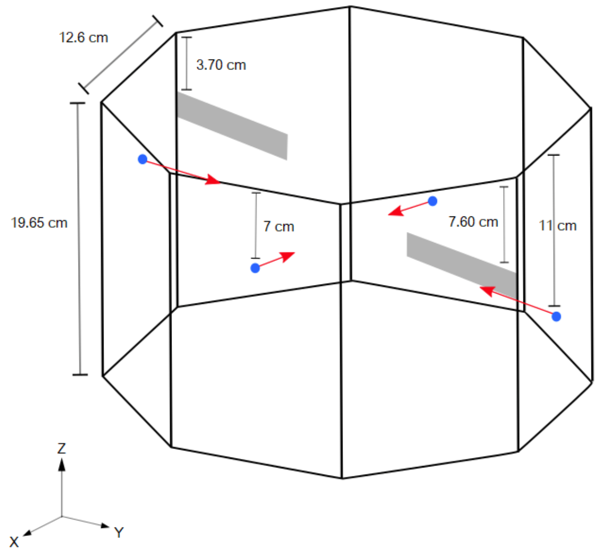

Figure 16: Octagonal Chamber (side view). Blue dots represent the monopole antenna positions and the red arrows represent their polarization. The two gray plates represent the FPEs

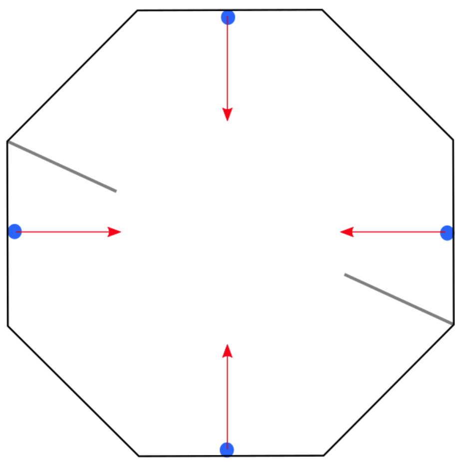

Figure 17: Octagonal Chamber (top view). Blue dots represent the monopole antenna positions and the red arrows represent their polarization. The two gray plates represent the FPEs

3.3 Characterization of the Object of Interest

In our experiments, the OI that was chosen for testing, was a demoisterized dry wooden sphere of 50 mm diameter shown in Fig. 18a. Fig. 18b shows the placement of the wooden OI inside the chamber hung by a non-conductive thread of length 6.2 cm from the top plate. A vector network analyzer (VNA) as well as a dielectric probe is used to measure the electrical properties of the object. For this purpose, a spherical wooden object that is identical to the OI was cut in half as shown in Fig. 19a so that it could be placed under the dielectric probe shown in Fig. 19b with the probe laying flatly on top of it.

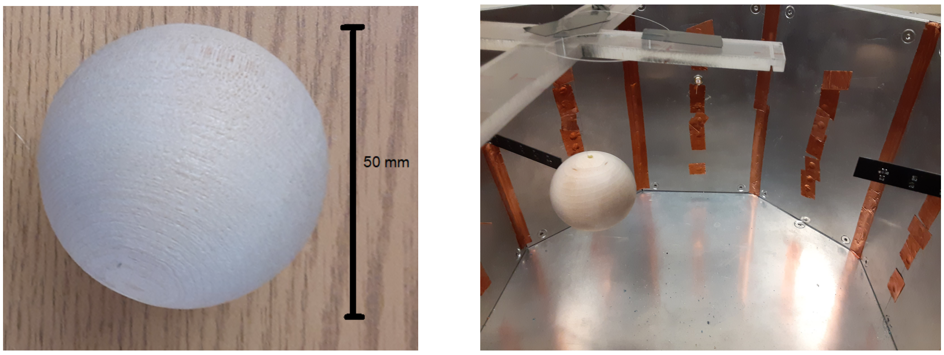

(a) Wooden Object used as OI **(b)** Wooden OI inside the Chamber

Figure 18: The wooden target and the placement of it within the imaging chamber

The VNA measures the electrical properties of the object, specifically ε' and ε''. Details on the method in which the properties are obtained can be found in [48, 49]. In order to make an accurate reading of the properties, the VNA must be calibrated with a known material such as water first. At which point the proper range of frequencies is selected (1 GHz - 2 GHz) and the probe is placed on the wooden object to perform measurements. From the S_{11} readings, the real and imaginary permittivity values are extracted for 101 frequency points across the frequency range.

(a) Wooden Object cut in half **(b)** Dielectric Probe

Figure 19: The wooden target and the dielectric probe used to measure its electrical properties

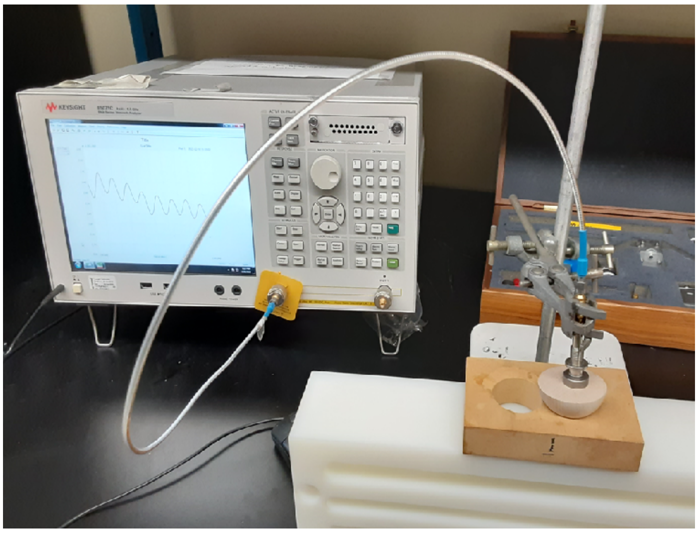

Figure 20: VNA set up to measure the electrical properties of the target

The following graphs show the measured values of ε' and ε'' obtained from the measurements. The object is considered homogeneous and its complex permittivity value is obtained from Eq. 8.

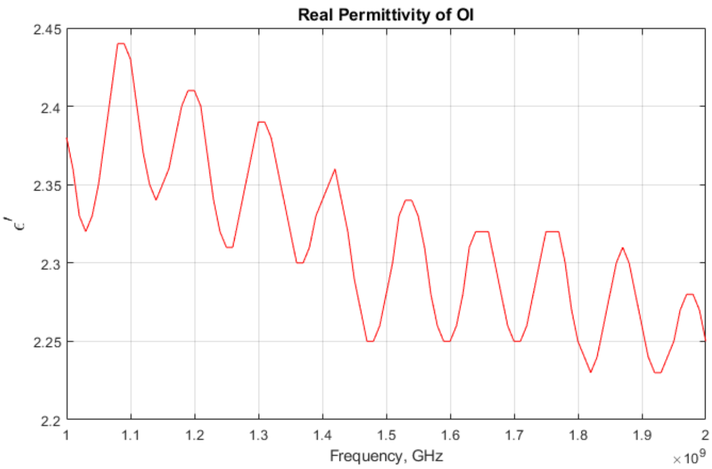

Figure 21: Real Permittivity of the Wooden OI over the 1 GHz - 2 GHz Frequency range

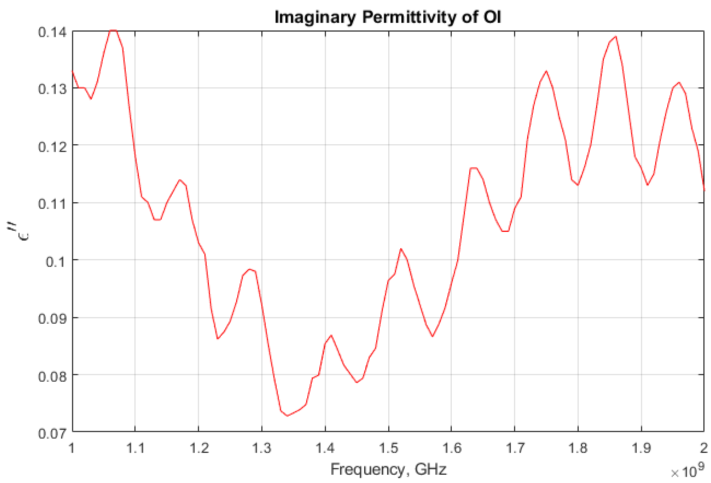

Figure 22: Imaginary Permittivity of the Wooden OI over the 1 GHz - 2 GHz Frequency range

Since we are utilizing a dielectric object of interest, it must allow sufficient wave penetration. As in our experimental measurements the frequency of operation is between 1 GHz - 2 GHz, it is essential to verify that there will be adequate interrogation energy into the target for optimized imaging. Equation below calculates the penetration depth based on frequency as well as electric and magnetic properties of the OI [50]:

$$\delta = \sqrt{\frac{2\rho}{\omega\mu}}\sqrt{\sqrt{1+(\rho\omega\epsilon)^2}+\rho\omega\epsilon} \tag{21}$$

Here, δ denotes the wave penetration in meters [m] to the depth where the interrogating field loses 37% of its initial power and ρ is the resistivity of the target. Using one of the exemplary inversion frequencies f = 1.15 GHz, and knowing the free space permeability $\mu_0 = 4\pi \times 10^{-7}$ [H/m], we can obtain the skin depth based on the above relation once the conductivity σ is calculated. Since our OI is considered to be non-magnetic, μ_r is assumed to be 1.

To calculate the resistivity ρ, of the material, first the electrical conductivity σ, must be obtained from which the resistivity can be calculated. For this purpose we make use of the Ampere's law as stated in Eq. 22. In the following equation, $\vec{\mathcal{J}}_c$ denotes the conduction current.

$$\nabla \times \vec{H} = j\omega\varepsilon_o\hat{\varepsilon}_r\vec{E} + \vec{\mathcal{J}}_c \tag{22}$$

The conduction current $\vec{\mathcal{J}}_c$ is defined as follow:

$$\vec{\mathcal{J}}_c = \sigma \vec{E} \tag{23}$$

Substituting (23) into (22) and factorizing the right hand side, we get:

$$\nabla \times \vec{H} = j\omega\varepsilon_o(\hat{\varepsilon}_r - j\frac{\sigma}{\omega\varepsilon_o})\vec{E} \tag{24}$$

Further simplifying; the right hand side can be written as:

$$j\omega\varepsilon_o(\varepsilon_r' + j\varepsilon_r'')\vec{E} \tag{25}$$

From the above relation, we can deduce a relationship between the electrical conductivity σ, and the imaginary permittivity ε'' as follow:

$$\varepsilon_r'' = -\frac{\sigma}{\omega\varepsilon_o} \tag{26}$$

From the above equation, conductivity σ, can be obtained. Resistivity ρ is calculated based on $\rho = 1/\sigma$. By substituting this value into Eq. 21, the penetration depth of the illuminating wave is calculated to be 59.31 [meters]. This means that the wave will fully penetrate into the object and adequate electromagnetic scattered field data will be collected at the receiver points.

To approximate the wave that reflects back due to impedance mismatch and to establish that there will be sufficient power entering the OI, the reflection coefficient is considered in order to obtain the percentage of power that is reflected at the surface and in turn retrieving the transmission coefficient. For this instance, plane wave incidence at normal is used as example.

$$\Gamma = \frac{\eta_2 - \eta_1}{\eta_2 + \eta_1} \tag{27}$$

Here, Γ is the reflection coefficient, η_2 is the impedance of the OI and η_1 is the impedance of the background that in our case is air. Choosing frequency of 1.15 GHz which is one of the inversion frequencies, and substituting the ε_r'' and ε_r' values obtained from Fig. 21 and Fig. 22 into Eq. 27, the reflection coefficient is calculated to be roughly -0.2. Substituting this value into Eq. 28, the transmission coefficient T, is calculated to be 0.8.

$$T = 1 + \Gamma \tag{28}$$

The power transmission coefficient $|T|^2$ will be 0.64 meaning that 64% of input power enters the OI. Considering both approximations discussed herein, it is concluded that there will be ample interrogation energy and sufficient power entering the OI.

3.4 VNA and Probe Driver Operation

For all our measurements in this research, we have utilized a 4-port Vector Network Analyzer (VNA) feeding the four probe chamber system. The VNA is the transceiver that allows us to transmit illuminating energy into the chamber and receive energy at each antenna. The VNA makes measurements in the form of S-parameters. Using only four antennas, relieves us from the need to use a RF switch multiplexer device or to use a VNA with higher number of ports. Fig. 23 shows the 4-port VNA (Agilent E5071C) used in this project.

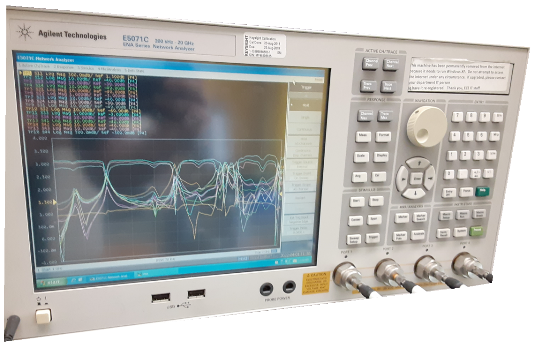

Figure 23: 4-port Vector Network Analyzer

Since utilization and reconfiguration of the FPEs is a major part of this design, a control device is utilized which allows us to set each FPE placed within the chamber to ON or OFF mode by sending a biasing voltage to the desired FPE. This device is called the probe driver and was designed by 151 Research Inc. [51].

The front panel of the device features 24 pin headers for connections to probes that are in this case FPEs. Each pin header can be connected to six probes. The positive

(a) Probe Driver device **(b)** DC Power Supply

Figure 24: The Power Supply and the MST Probe Driver

voltage lead from a FPE is connected to the top row of the desired column (one through six) and the negative voltage lead from a FPE is connected to the bottom row of the same column to ensure proper biasing. The back of the device features a USB connection to the internal microcontroller, and banana jack connection to the BK Precision 1687B power supply which is a DC power supply with the desired voltage setting required to power the probe driver.

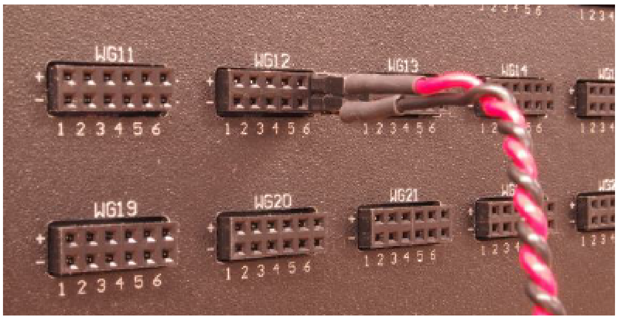

Figure 25: Close up of the front panel of the probe driver and pin connections

Communication with the probe driver is done over the USB port on the back panel. Power for the internal circuitry is also provided over this port. The probe driver is connected to a command computer with a serial terminal application (e.g. PuTTY) with a USB cable and commands are sent to the device in the form of 32 digit binary code specifically activating the desired pins. For example, in order to set the FPE that is connected to the pin showing in Fig. 25, the code that is sent to the probe driver is as follow:

“00000000000100000000000000000000”

Considering Fig. 25 as an example, the pin to be activated is the sixth pin on WG12. In the binary code shown above, the first six characters refer to the pins on WG11, the second six characters refer the pins on WG12 and so on. To activate each pin using the binary code, the binary character referring to that pin is set to “1”, while other characters are set to “0”. Therefore, the binary code to activate the above pin shown in Fig. 25 is the 32 digit code shown above.

The voltage of the BK Precision supply can be set manually to voltages from 0.8 V to 36.2 V. For this experiment the voltage is set to between 6.5 V and 9 V. The overall setup is shown in Fig. 26.

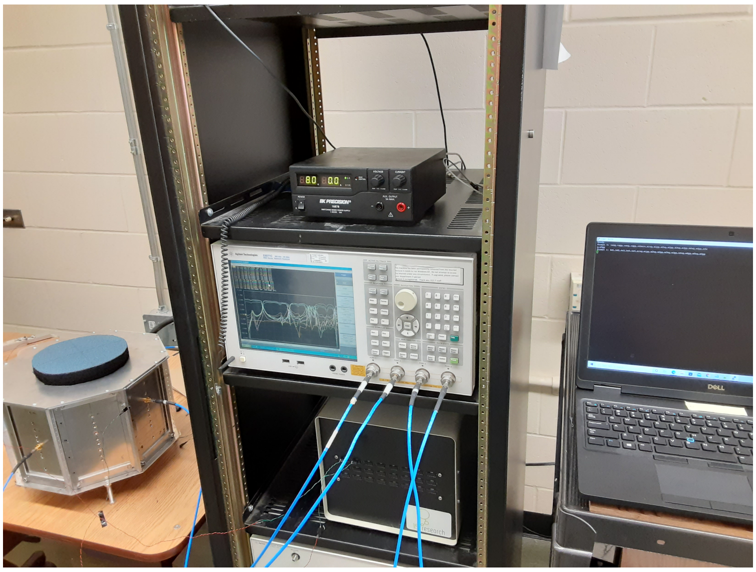

Figure 26: Overall Setup showing the probe driver, the VNA, the chamber as well as the control computer

As shown in the above picture, the four coaxial cables are connected to the four ports on the VNA on one end and to the monopole antennas inside the chamber on the other end. The cables are calibrated to make sure that they are in phase. The Precision power supply is also shown that is connected to the probe driver. The FPEs placed in the chamber are connected to the pins on the front panel of the probe driver device that is controlled by the command computer.

Chapter 4

Proof of Concept and Simulations

4.1 Proof of Concept

As described in the previous chapters, different combinations of FPE patterns of ON/OFF give rise to varying EM fields within the chamber without the need to modify and manipulate the Tx-Rx pairs and/or the chamber to create more non-redundant data. To this end, a brief experiment was conducted to verify that varying experimentally collected fields are observed when toggling FPEs between ON and OFF modes.

To investigate the proper operation of the field perturbing elements, two FPEs were placed on either end of the chamber across from each other at the same height from the top surface. Two magnetic or electric field probes were placed on opposite walls of the chamber, 90 degrees along the circumference to where the FPEs are located, to act as transmitter as well as collect the data. For this experiment both E-Fields and H-Fields were collected in the frequency range 1 GHz - 3 GHz. Fig. 27a shows the setup for the case with monopole E-field probes to collect the E-Fields. In the numerical FEM model the transmitting probes are modelled as point sources. The chamber includes a metallic top with a circular hole that is covered by an absorbing foam during measurements. The empty circular top is modelled as an absorbing boundary condition (ABC) and is shown in Fig. 27b. Fig. 28[1] shows a direct comparison, in dB, of the fields with the FPEs in different modes in an empty chamber for both synthetically and experimentally collected data.

[1]Note that in Fig. 28, the synthetic plots show the field quantities while the experimental plots show the S_{21} values. For convenience in comparison they are plotted in the same graph.

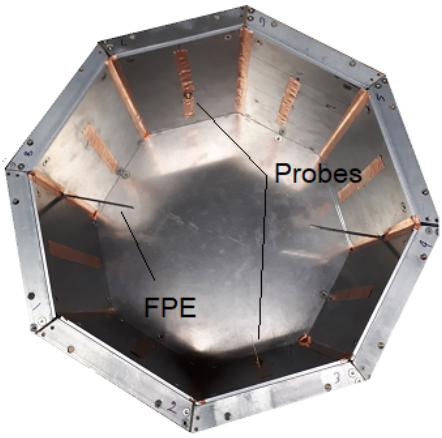

(a) Octagonal metallic measurement chamber

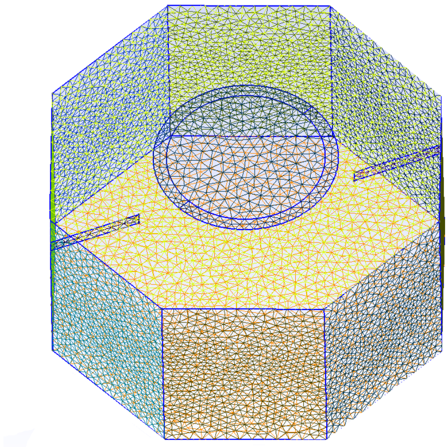

(b) Numerical chamber showing the top modelled as ABC

Figure 27: Two-probe setup to inspect the effect of FPEs

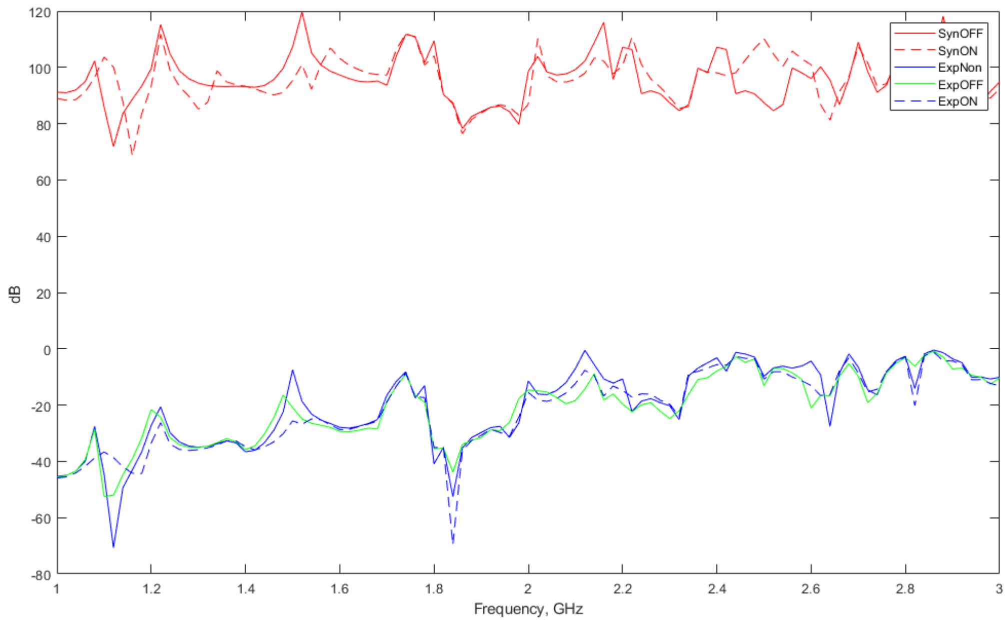

Figure 28: Numerical (field values) vs. experimental (S_{21}) in different FPE modes (ON/OFF) for frequency 1GHz - 3GHz. SynOFF shows the synthetic case where FPE is in OFF mode and SynON shows the same with FPE in ON mode. ExpNon shows the measured field with no FPE in the chamber. ExpOFF shows the measured field with FPE in OFF mode and ExpON shows the measured fields with FPEs in the ON mode

It is clearly observed that the measured fields follow very similar patterns as the synthetically collected fields which validates the model and also confirms that FPEs that are ON/OFF can be modelled by thin PEC surfaces or no surfaces, respectively, in the FEM algorithm. Moreover, the change in the collected fields once the FPE mode is toggled is clearly visible which further shows that this is a viable technique to modify the field within the chamber.

Fig. 29 shows the experimentally measured S_{21} fields in three different modes. First, when there are no FPEs present in the chamber. Second, when the two FPEs are in reversed biased/passive mode (OFF). And third, when they are in the forward biased/active mode (ON). It can be deduced from the figure below that the FPE mode has a readily observable effect on the field within the chamber. That is, the field within the chamber is considerably different when the FPE is in active mode as compared with when it is in the passive mode.

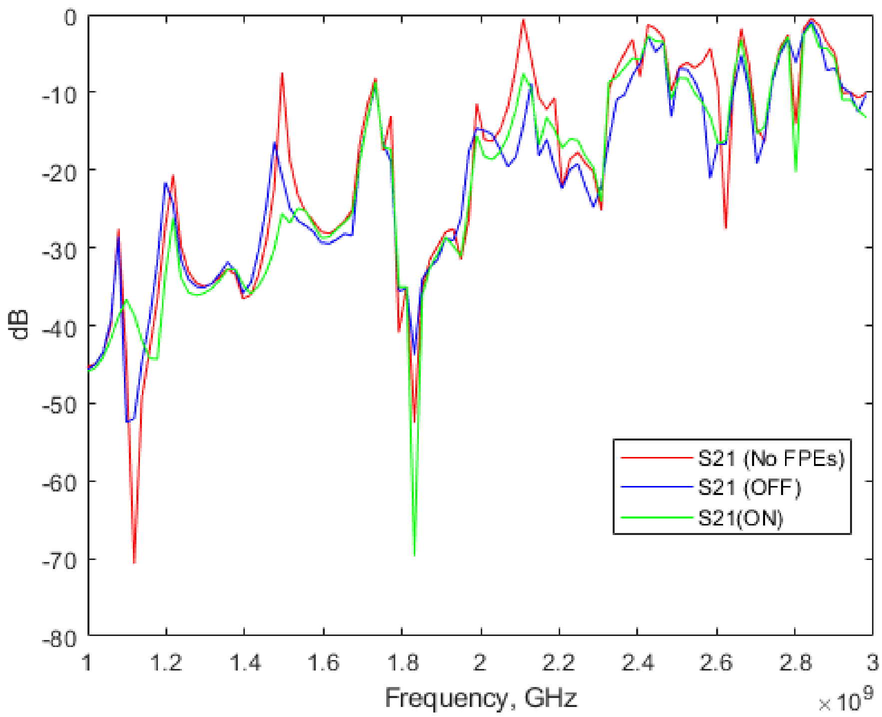

Figure 29: Measured S_{21} for different modes of the FPEs in the frequency range 1GHz - 3GHz. Red plot shows the case with no FPEs in the chamber, Blue plot shows the case when FPEs are in OFF mode and the Green plot shows the case with the FPEs in ON mode

4.2 Synthetic Analysis of the Field Distribution

In order to further evaluate the efficacy of the FPEs and their ability to alter the field distribution inside the enclosure, a numerical analysis was conducted with the chamber being modelled to the size of the actual measurement chamber and two FPEs placed in the same position within the chamber as in the experimental case. As stated previously, in the FEM forward solver, for the case where an FPE is in the ON position it is modelled by a PEC surface. For the case that the FPE is in the OFF position, it is modelled as non existent.

The different cases of FPEs being in different modes within an otherwise empty chamber were modelled using the forward FEM solver the results were input in PARAVIEW to get a visual on the field distribution in different states of FPE combinations. The fields were simulated at several frequencies in the bandwidth of interest and two exemplary frequencies: 1.13 GHz and 1.15 GHz, are here looked at in more detail.

It is shown that fields in two different frequencies due to the excitation of the model with a ρ-directed monopole (that is modelled by a point source) differ significantly which is another testament to frequency dependence of MWI particularly in a metallic enclosure. It is also observed that the field is altered substantially when the mode of the reconfigurable plate is toggled. Fig. 30 and Fig. 31 show the change in field distribution in magnitude and phase of the fields in different FPE modes and frequencies. Electric field distribution in $\hat{z}$ and $\hat{y}$ polarizations are shown when one of the ρ-directed monopole E-field probes is transmitting.

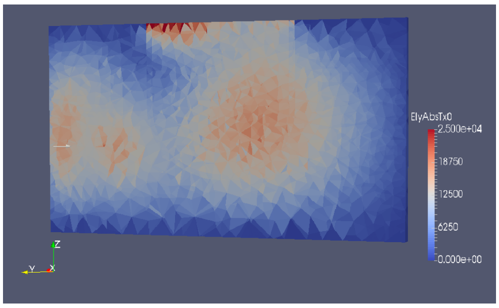

(a) E_y, Magnitude (OFF)

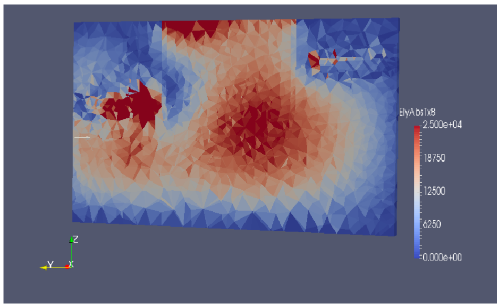

(b) E_y, Magnitude (ON)

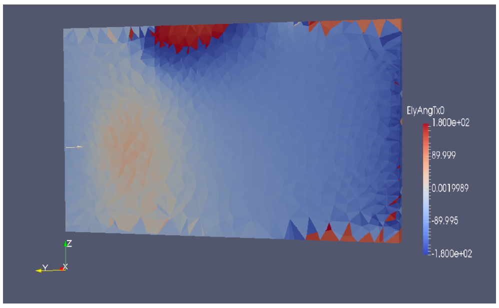

(c) E_y,Phase (OFF)

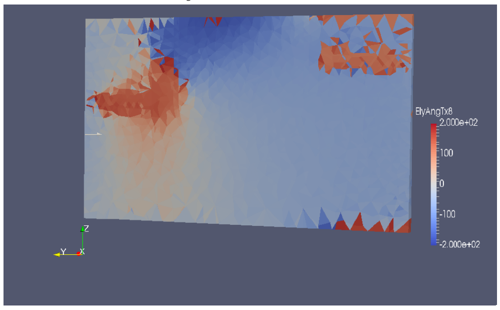

(d) E_y,Phase (ON)

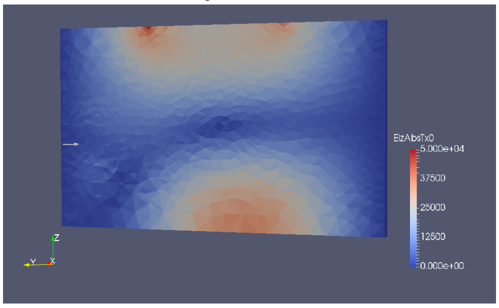

(e) E_z, Magnitude (OFF)

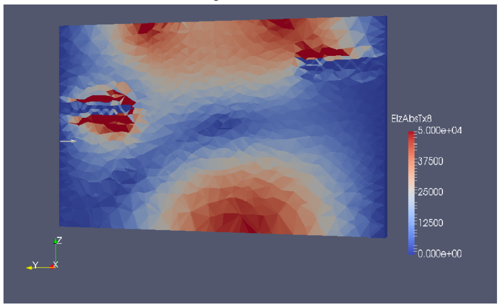

(f) E_z, Magnitude (ON)

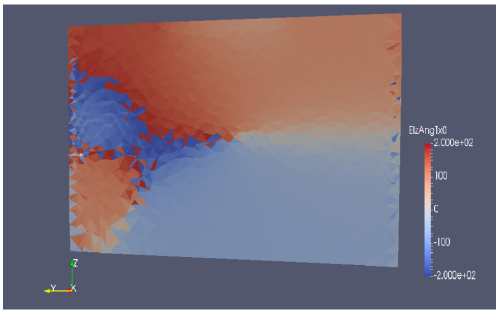

(g) E_z, Phase (OFF)

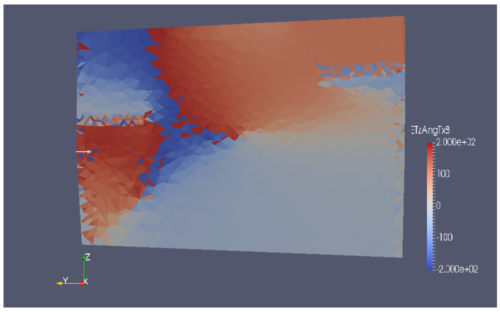

(h) E_z, Phase (ON)

Figure 30: Magnitude and phase of the E_y and E_z inside a metallic enclosure when E_ρ is excited when dynamic boundaries are in (a,c,e,g) passive/OFF mode and (b,d,f,h) active/ON mode at 1.13GHz

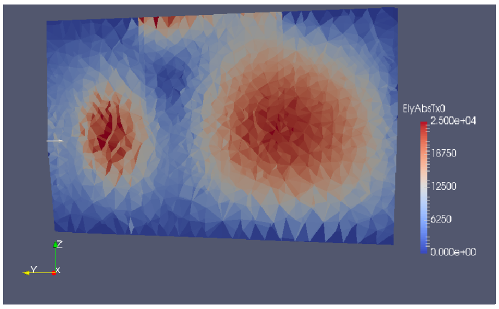

(a) E_y, Magnitude (OFF)

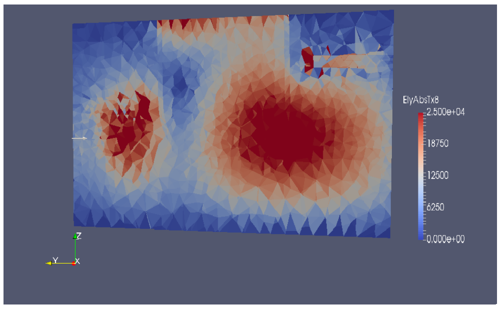

(b) E_y, Magnitude (ON)

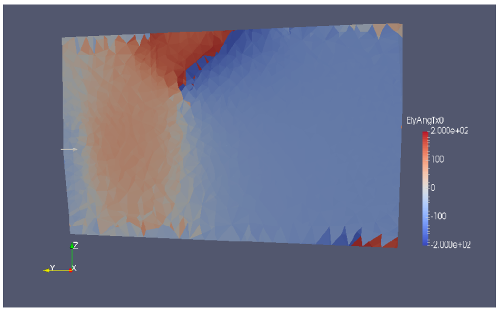

(c) E_y,Phase (OFF)

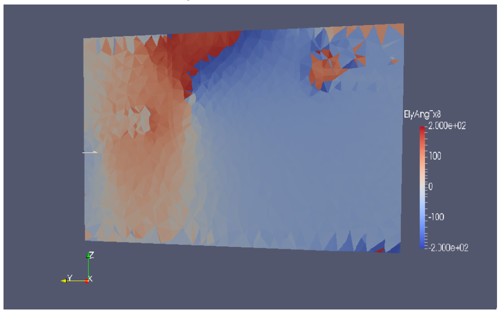

(d) E_y,Phase (ON)

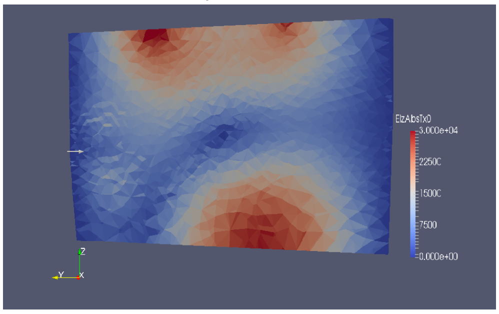

(e) E_z, Magnitude (OFF)

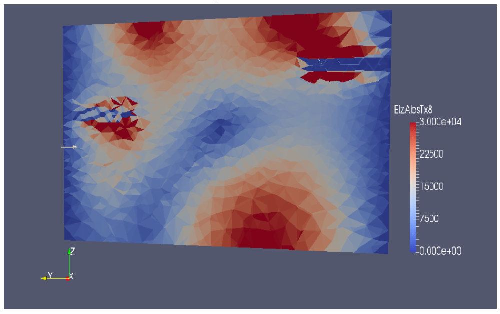

(f) E_z, Magnitude (ON)

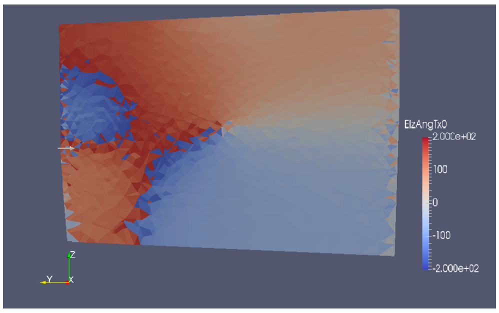

(g) E_z, Phase (OFF)

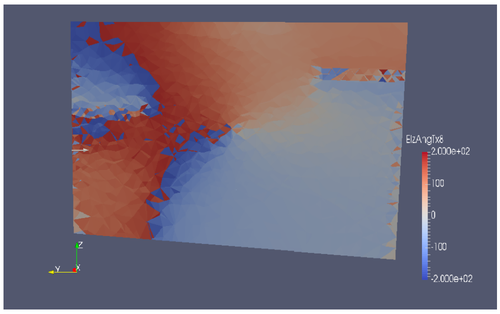

(h) E_z, Phase (ON)

Figure 31: Magnitude and phase of the E_y and E_z inside a metallic enclosure when E_ρ is excited when dynamic boundaries are in (a,c,e,g) passive/OFF mode and (b,d,f,h) active/ON mode at 1.15GHz

It is noted from the above diagrams that both magnitude and the phase of the field distribution inside the chamber are changed when the mode of the dynamic boundary elements are toggled (active/passive). It is also noted that the field distribution is significantly different in the two frequencies due to the metallic and resonant nature of the enclosure that is modelled as PEC in this numerical experiment.

Looking at Fig. 30a and Fig. 31a when the FPEs are modelled as non-existent, the field distribution of the magnitude of E_y is considerably different at the two frequencies. That is, the field is more intense at 1.15 GHz than at 1.13 GHz. A similar comment can be made for the field distribution of the magnitude of E_z, that it is also more intense at 1.15 GHz when the FPEs are modelled as passive. When the FPEs are in the active mode however, the magnitude of the field is of higher intensity at 1.13 GHz.

Fig. 30h and Fig. 31h show the field distribution of the phase of E_z within the chamber at 1.13 GHz and 1.15 GHz respectively. As shown in the diagrams, the phase variations surrounding the FPEs at 1.13 GHz is significantly higher than the phase variations at 1.15 GHz. A similar observation is true for the phase of E_y. Comparing the field distributions at the two frequencies considered herein, it can be deduced that toggling the FPE modes have a clear and observable effect on the field distribution on both magnitude and phase. This effect however, is more significant at the frequency of 1.13 GHz compared with 1.15 GHz.

4.3 Simulation Setup

In order to be able to validate the feasibility of the FPE technique and to gather applicable evidence that utilizing FPEs to increase the amount of collected data will in fact enhance the accuracy of permittivity reconstruction of the OI, a series of numerical tests were performed using FEM-CSI.

A synthetic octagonal chamber similar to the actual enclosure but with shorter side lengths was designed with 16 FPEs positioned inside it. The OI in this case was a sphere of 55 mm diameter positioned 2.5 cm off-center and is positioned at 2.65 cm from the top surface of the chamber. The height of each of the side walls are 15.65 cm and the four receivers are positioned on four walls across from each other. Numerical data was collected in normal E-field polarization and was inverted on five frequencies to obtain permittivity reconstruction of the OI.

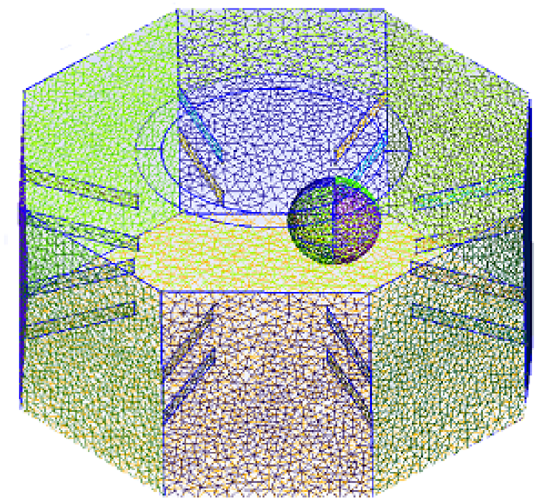

Figure 32: Schematic depiction of the 16 FPEs and the target with the chamber with side walls with the height of 15.65 cm and length of 12.14 cm

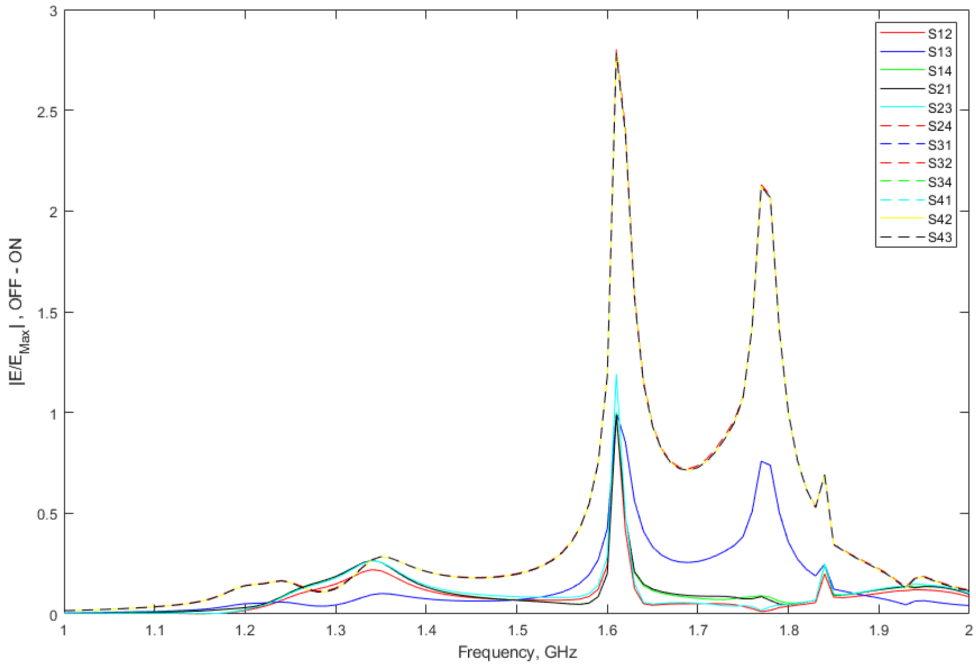

Figure 33: Difference in the FPEs OFF/ON mode of the synthetically collected fields utilizing four antennas in the empty chamber for all Tx-Rx pairs in the frequency range 1 GHz - 2 GHz

The above figure shows the difference between the synthetically collected fields in two modes: first, when the FPEs are in OFF mode (modelled as non-existent) and second, when two FPEs are in ON mode (modelled as PEC plates) for all Tx-Rx pairs in the empty chamber. Five frequency points were selected based upon Fig. 33. The frequencies to attempt inversions at were selected to be the ones with the greatest change in the magnitude of the collected fields when the FPEs are toggled OFF/ON. The y-axis shows the difference between the OFF mode and the ON mode while the x-axis portrays the frequency range 1 GHz - 2 GHz. The goal is to select frequencies where the collected field data showing the difference between the OFF and ON mode follows the same pattern for all or most of the Tx-Rx pairs. Therefore, the selected frequency points based on the above criteria are 1.07 GHz, 1.12 GHz, 1.36 GHz and 1.61 GHz and 1.84 GHz.

Table (1) shows the details of the numerical design setup:

Total number of transmitters	4
Total number of receivers	3
Total number of FPEs	16
Number of FPE configurations	16
Total amount of data	192
Total number of Tetrahedra	95551
Tx/Rx polarization	E-Normal
Target permittivity	2.0-j0.2
Background permittivity	1.0-j0.001

Table 1: Numerical Inversion Details

4.4 Numerical Inversion Results

In this section numerical inversion results are presented for the five frequencies selected based upon the above criterion. Figures on the left show the case where no FPEs are used with the total amount of data being 12 (S_{ii} removed). Figures on the right hand side show the case where 16 configurations of the FPEs are utilized giving rise to total amount of data of 192. The results are shown for each of the five frequency points individually for comparison. The final reconstructed permittivity map is thresholds for each frequency so that the target can be easily distinguished.

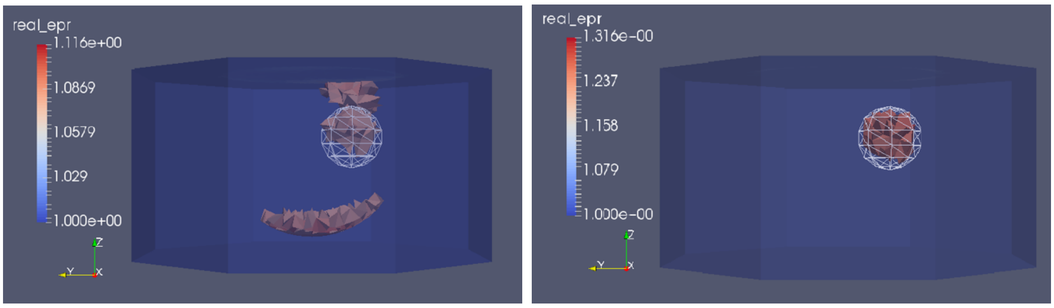

Figure 34: F = 1.07GHz, Left: No FPEs utilized, Right: 16 FPEs combination. Threshold set from 4% below the maximum to the maximum permittivity

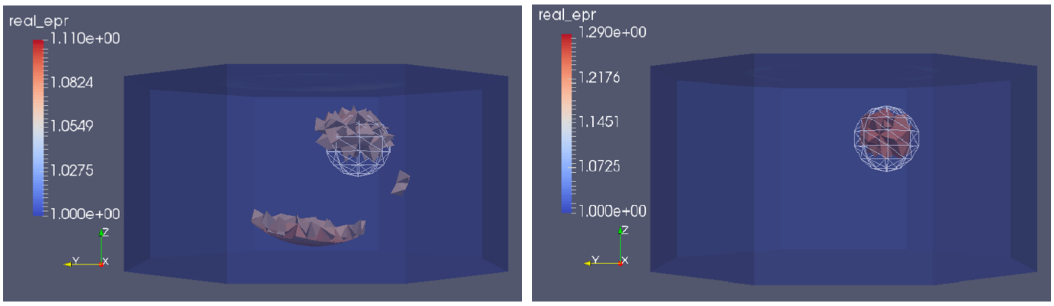

Figure 35: F = 1.12GHz, Left: No FPEs utilized, Right: 16 FPEs combination. Threshold set from 4% below the maximum to the maximum permittivity

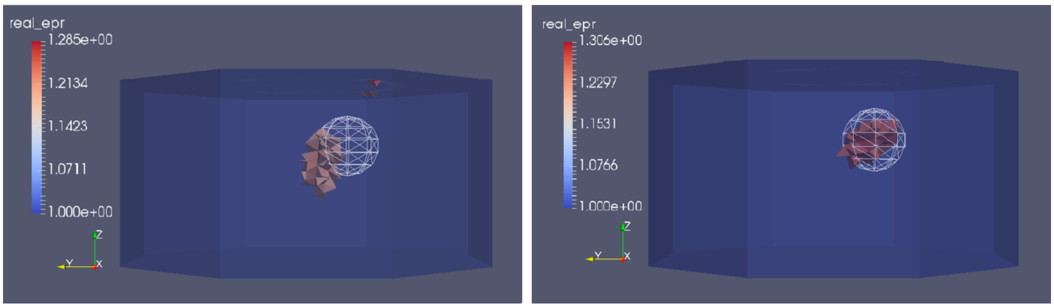

Figure 36: F = 1.36GHz, Left: No FPEs utilized, Right: 16 FPEs combination. Threshold set from 8% below the maximum to the maximum permittivity

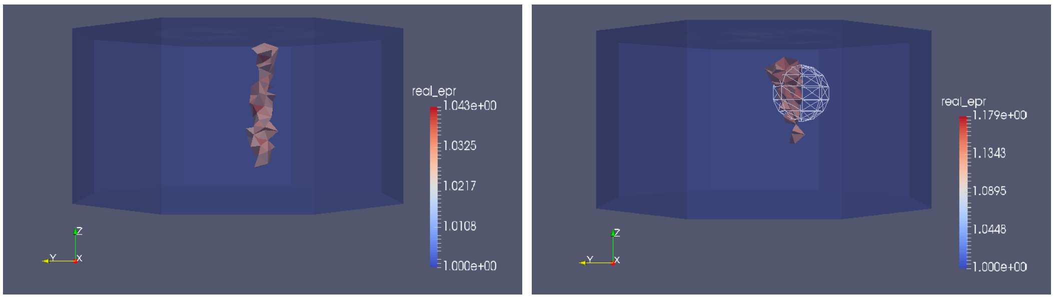

Figure 37: F = 1.61GHz, Left: No FPEs utilized, Right: 16 FPEs combination. Threshold set from 3% below the maximum to the maximum permittivity

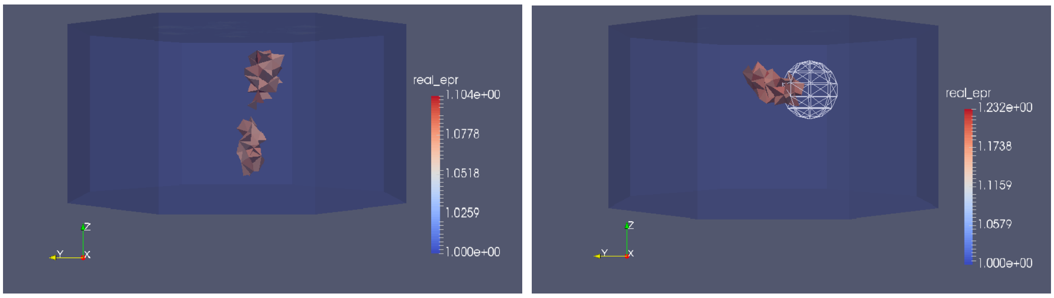

Figure 38: F = 1.84GHz, Left: No FPEs utilized, Right: 16 FPE combination. Threshold set from 6.5% below the maximum to the maximum permittivity

From the simulation results it can be clearly deduced that increasing the amount of non-redundant data by the use of FPEs is attainable and there is significant improvement to the image when utilizing the increased amount of data with the incorporation of the FPE combinations.

In addition, it is observed from the above figures that the frequency dependency of the results is still significant where for instance at frequency of 1.61 GHz there are no meaningful enhancement of the image. We see that at 1.84 GHz the improvement is minimal whereas most of the observable imaging performance enhancement has have taken place in the lower frequency spectrum, specifically at 1.07 GHz and 1.12 GHz.

Based on Fig. 33, the frequencies where we have a meaningful improvement in the OI reconstructions are the ones that the difference in the OFF/ON modes are consistent and close between all Tx-Rx pairs. Examples of this would be at frequencies 1.07 GHz, 1.12 GHz and 1.36 GHz where the reconstructed permittivity of the OI is considerably more accurate for the case when the FPEs are being utilized compared with the case when no FPEs are incorporated.

At frequencies where a subset of Tx-Rx pairs dominate the interrogation energy, there are no meaningful improvements in the target reconstruction due to dominating data-error by those Tx-Rx pairs. Examples of these frequencies are 1.61 GHz and 1.84 GHz. At those frequencies, there are still observable changes in the reconstructed permittivity map due to the varying field distribution within the enclosure and the more independent data that is generated but the reconstructions do not pinpoint the location of the OI the same way as in the mentioned lower tier frequencies.

The focus of this chapter was first to prove that placement of the field perturbing elements within the metallic resonant chamber will change the field distribution within the enclosure. For this purpose, a number of experiments were performed to confirm the changes in field distribution due to utilization of FPEs. The second focus was to synthetically show that the variations in the field distribution will lead to generation of more independent data which ultimately leads to enhancement in the imaging performance and reconstruction of the OI.

Chapter 5

Experimental Results

In this chapter, the experimental setup and inversion results as well as the modelling approach, frequency selection and data calibration are presented and discussed. For the experimental system, the chamber with side walls of height 19.65 cm and length 12.14 cm has been designed and utilized. Four monopole E-field probes as well as two FPEs are placed in the chamber as shown in Fig. 39. The wooden target (OI characteristics described in detail in chapter 3.3) was placed in two different positions diagonally at 2 cm off-center and at the height of 6.2 cm from the top surface of the chamber. A numerical model of the full sized chamber has been developed with the probes and FPEs in the exact same positions as in the experimental chamber.

In the following sections, the frequency selection procedure and criteria based on the match between the measurement system and the numerical model is discussed and analyzed. Based on the chosen frequency points, a calibration procedure is also discussed in the following section which discusses calibrating the measured data with those of the synthetically collected ones. Finally the inversion results are presented showcasing the effectiveness of the FPE technique in permittivity reconstruction of the OI.

5.1 Frequency Selection and Modelling Error

It is well observed that MWI in metallic imaging chambers is highly frequency dependent where slightest perturbations inside the chamber creates vastly different collected fields. Thus, as the frequency selection criterion, it is of considerable importance for

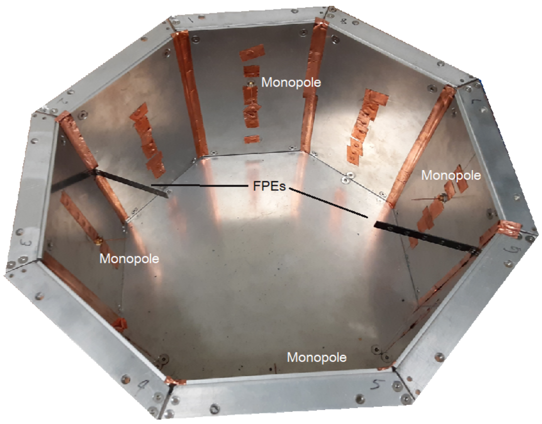

Figure 39: Experimental chamber incorporating four monopole E-field probes as well as two FPEs

data to be collected at frequency points where there is significant match between the incident fields with different combinations of FPEs. In other words, the measured fields inside the chamber in the absence of the OI must match closely with those of the synthetically collected fields with the absence of the OI for as many of the Tx-Rx pairs as possible.

For this purpose, experimental incident field data were collected at 101 frequency points in the range of 1 GHz - 2 GHz in 10 MHz increments and compared with those of the synthetically collected fields with all three combinations of the FPE modes. Specifically, the first combination is when both FPEs are in OFF mode. In the second combination, one FPE is set to ON while the other remains in OFF mode. In the third combination, both FPEs are set to ON mode.

Utilizing the four probes in the chamber and without the inclusion of the FPEs, the total number of collected data equals the number of transmitters, nTx, multiplied by the number of receivers, nRx, (nTx $\times$ nRx = 16). When all three combinations of the FPEs are incorporated, the total number of collected data for the target at each position is multipled by the number of FPE combinations, nFPE, and will be equal to nTx × nRx × nFPE = 4 × 4 × 3 = 48. For each round of data collection cycle, the S_{ii} terms are ignored therefore the total number of independent data utilizing FPEs will be 48 - 12 = 36 and without utilizing them will be 16 - 4 = 12. It is noted that this is a relatively small amount of data to perform 3-D inversions, but the target is a simple sphere and the point of this exercise is to validate that using FPEs can increase the amount of independent data resulting in improved imaging.

One round of data collection is performed for each FPE combination resulting in three times the amount of non-redundant data collected. The resulting incident field data are compared and it is determined that at the following frequency points the correlation coefficient between the measured and numerical incident fields are higher than 65%: 1.13 GHz, 1.14 GHz, 1.15 GHz, 1.16 GHz, 1.86 GHz and 1.87 GHz.

Correlation coefficient values which have been calculated on the magnitudes of the field are obtained based on the following relation:

$$\rho(A,B) = \frac{1}{N-1}\sum_{n=1}^{N}(\frac{A_i-\mu_A}{\sigma_A})(\frac{B_i-\mu_B}{\sigma_B}) \tag{29}$$

Here, A is the measured S-parameter and B is the synthetically collected incident field. Both collected fields are normal component of the electric field. μ and σ are the mean and standard deviation respectively.
The following figures compare the normalized measured vs. numerical incident fields at the aforementioned frequency points.

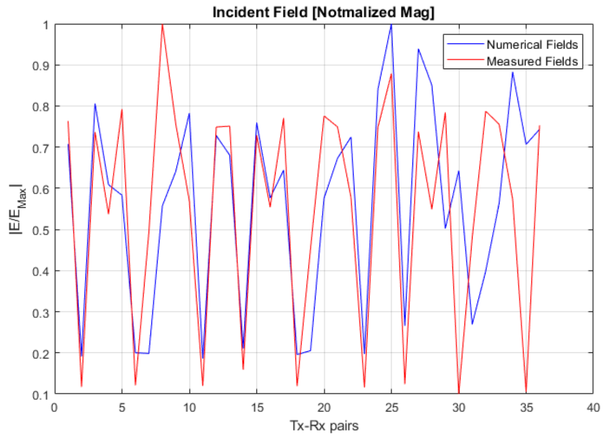

(a) F = 1.13GHz

(b) F = 1.14GHz

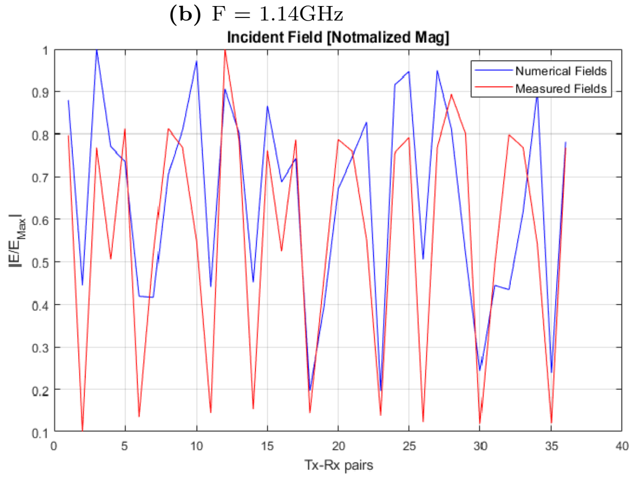

(c) F = 1.15GHz

Figure 40: Measured vs. Numerical incident fields for frequencies 1.13 GHz, 1.14 GHz and 1.15 GHz. Measured and Numerical data are depicted by red and blue plots respectively

(a) F = 1.16GHz

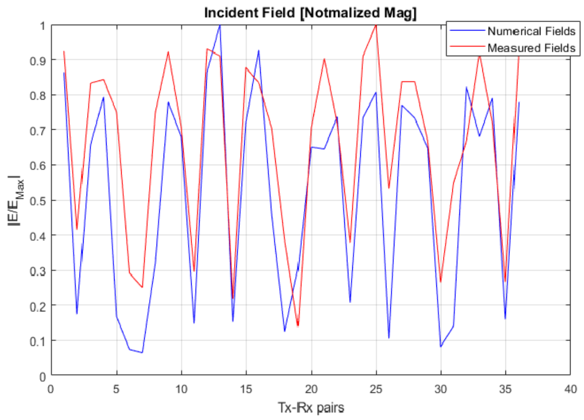

(b) F = 1.85GHz

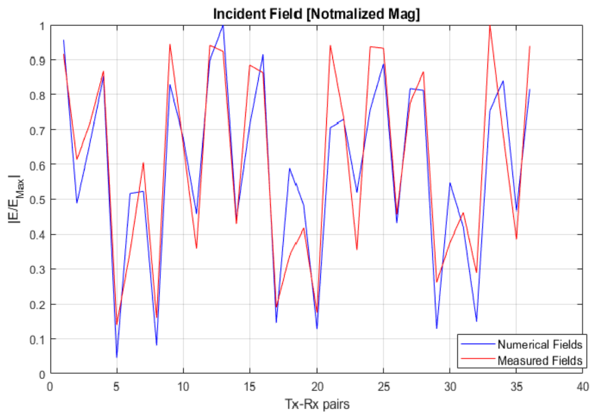

(c) F = 1.86GHz

Figure 41: Measured vs. Numerical incident fields for frequencies 1.16 GHz, 1.86 GHz and 1.87 GHz. Measured and Numerical data are depicted by red and blue plots respectively

In the above figures, the x-axis shows the transmitter-receiver (Tx-Rx) numbers with the S_{ii} terms ignored. We utilize two FPEs in three combinations. The first combination being where both FPEs are in OFF mode. In the second combination one FPE plate is in OFF mode while the other is in ON mode and in the third combination, both FPEs are set to ON mode. The first 12 numbers on the x-axis show the first FPE combination with both FPEs being OFF. 13 - 26 are for the case when one FPE is ON while the other is OFF. Finally the Tx-Rx pairs from 27 - 36 refer to the third combination where both FPEs are ON. The y-axis depicts the normalized magnitude of the incident fields.

Table (2) presents the correlation coefficient values at each frequency between the measured and synthetic incident fields:

Frequency, GHz	Correlation Coefficient
1.13	0.7511
1.14	0.6742
1.15	0.7533
1.16	0.7063
1.85	0.8239
1.86	0.8337

Table 2: Correlation coefficients between simulated $E^{inc,sim}$ and measured fields $E^{inc,meas}$ at six frequency points

5.2 Calibration

When comparing the experimentally collected data to the synthetic ones, there are always some mismatches between the measurement system and the numerical model. For instance the mismatch includes the fact that measurements collect voltages at the ends of antenna/cable systems whereas the numerical models output field values.

In addition there will be inaccuracies in modelling boundary conditions and the dielectric properties of the target being modelled. The accuracy of the model itself can be improved by either creating a more complex numerical model [52] or by designing a less complex experimental system. Increasing the complexity of the numerical model can dramatically raise the computational burden. So the next option is to reduce the complexity of the imaging system by reducing the number of sources and receivers and/or by utilizing simple probes and chambers that can be easily modelled. In the end, the experimental data must still be calibrated, but the effectiveness of the calibration and the resulting imaging results will be much improved if the modelling error is low.

There are two major techniques for calibrating the experimentally measured data inside an imaging chamber when utilizing a homogeneous background [34, 53]:

- "Incident Field Calibration" shown below in Eq. 30
- "Scattered Field Calibration" shown below in Eq. 31

$$E_{r,t}^{sct,cal} = \frac{E_{r,t}^{inc,empty}}{U_{r,t}^{inc,empty}} (U_{r,t}^{tot,OI} - U_{r,t}^{inc,empty}) \tag{30}$$

$$E_{r,t}^{sct,cal} = \frac{E_{r,t}^{sct,calobj}}{U_{r,t}^{tot,calobj} - U_{r,t}^{inc,empty}} (U_{r,t}^{tot,OI} - U_{r,t}^{inc,empty}) \tag{31}$$

Here, the calibrated scattered field values are provided for a given transmitter t and receiver r. $E_{r,t}^{sct,cal}$ is the calibrated scattered field, $E_{r,t}^{inc,empty}$ is the simulated incident field (empty chamber), $U_{r,t}^{inc,empty}$ is the measured incident field (empty chamber), $U_{r,t}^{tot,OI}$ is the measured total field in presence of the OI, $E^{sct,calobj}$ is the simulated scattered field for the calibration object and $U_{r,t}^{tot,calobj}$ is the measured total field for the calibration object.

When utilizing reconfigurable FPEs, one round of data is collected for each combination of the FPE mode. As described earlier, we utilize three FPE combinations therefore three rounds of data collection cycles are performed. The individual data sets are then added together leading to an increased amount of overall independent data which is ultimately input in the calibration algorithm that is based on Eq. 30. Given that the OI is imaged against a homogeneous air background for the experiments performed herein, we have made use of incident field calibration which eliminates the need for utilizing additional calibration objects.

5.3 Inversion Results

To evaluate the performance of the FPE methodology, experimental tests were performed utilizing the imaging setup shown in Fig. 26. Data was collected and inverted at two frequencies, 1.13GHz and 1.15GHz, at two different OI positions and for two different cases. First, for the case where there are no FPEs present in the chamber and second, for the three FPE configurations providing us with three times the amount of data. Table (3) shows the computational requirement for each of these inversions:

Number of Bkg Tetrahedra	Iteration Count [s]	Amount of Data	Time per Iteration	Total Inversion Time
93244	300	12	5.6	00:00:26
93244	300	36	17.20	00:01:27

Table 3: Required computational resources for 300 iteration inversion of discretized mesh on 32 cores

The following figures present the experimental inversion results and compare the two cases, with and without FPEs, and their effects on the final reconstructed permittivity map of the OI. The diagrams below show the 3-D inversion results for the spherical wooden OI that its real and imaginary permittivity values are given in plots of Fig. 21 and Fig. 22. According to the plots, the complex permittivity of the OI at 1.13 GHz and 1.15 GHz is approximately 2.33 - j0.11. The diagrams below show the results from different angles at the two frequency points being considered. Note that the permittivity reconstructions are thresholded and the threshold percentage is given for each frequency in the following figures.

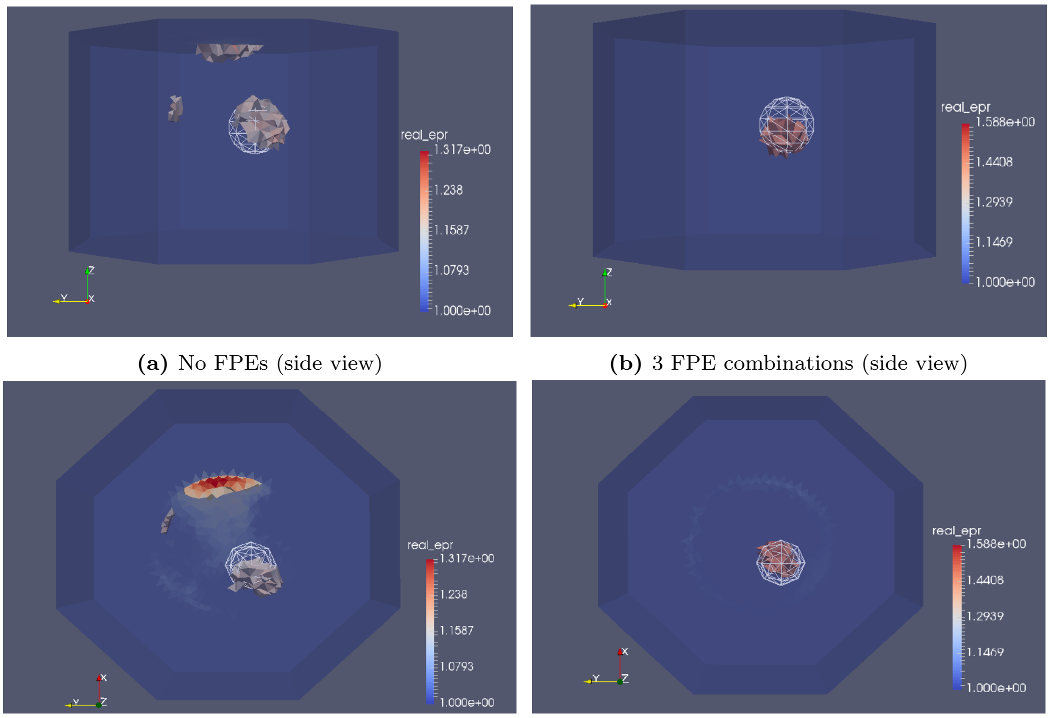

(a) No FPEs (side view) **(b)** 3 FPE combinations (side view)

(c) No FPEs (top view) **(d)** 3 FPE combinations (top view)

Figure 42: Experimental inversion results at 1.13GHz for the target at Position 1. (a,c) are the case where no FPEs are incorporated whereas (b,d) are the case where 3 FPE combinations are utilized. Threshold set from 12.5% below the maximum to the maximum permittivity. (dashed sphere shows the approximate position of the target)

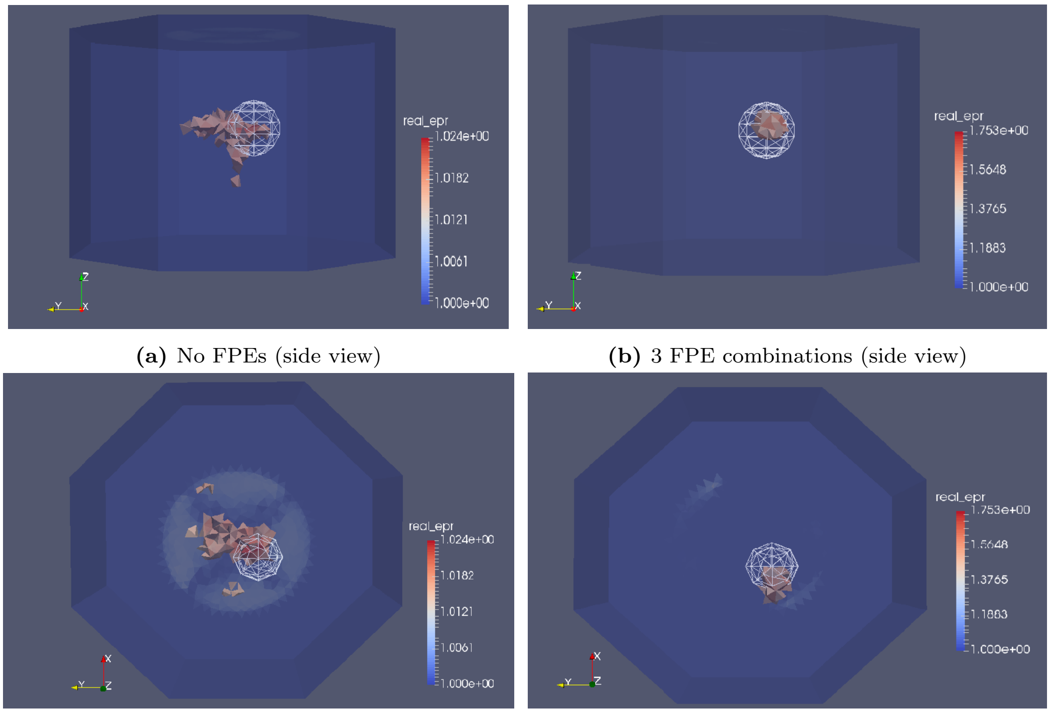

(a) No FPEs (side view) **(b)** 3 FPE combinations (side view)

(c) No FPEs (top view) **(d)** 3 FPE combinations (top view)

Figure 43: Experimental inversion results at 1.15GHz for the target at Position 1. (a,c) are the case where no FPEs are incorporated whereas (b,d) are the case where 3 FPE combinations are utilized. Threshold set from 18% below the maximum to the maximum permittivity. (dashed sphere shows the approximate position of the target)

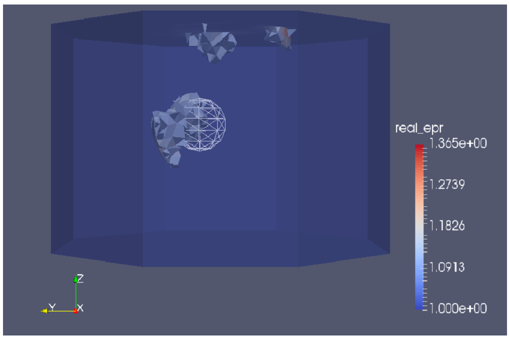

(a) No FPEs (side view)

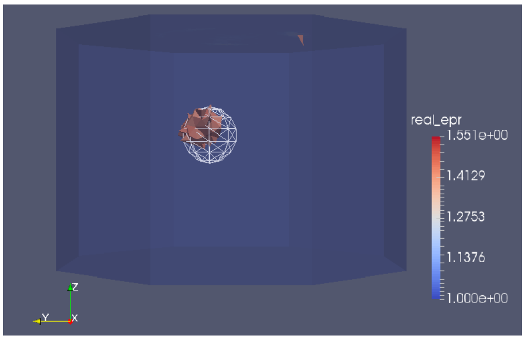

(b) 3 FPE combinations (side view)

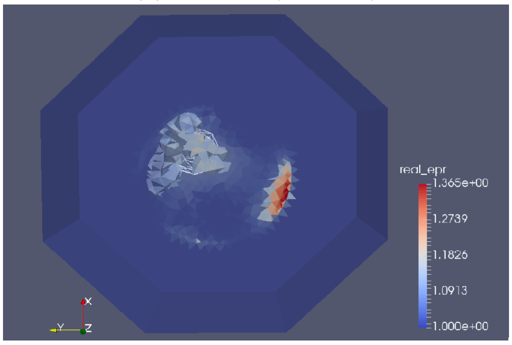

(c) No FPEs (top view)

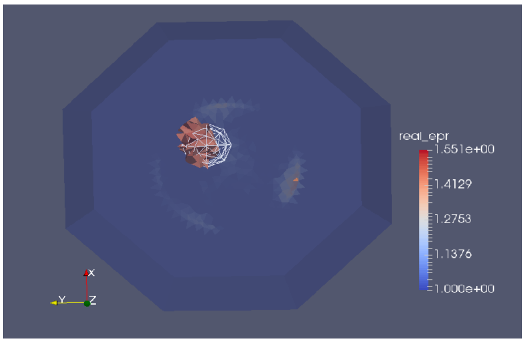

(d) 3 FPE combinations (top view)

Figure 44: Experimental inversion results at 1.13GHz for the target at Position 2. (a,c) are the case where no FPEs are incorporated whereas (b,d) are the case where 3 FPE combinations are utilized. Threshold set from 11% below the maximum to the maximum permittivity. (dashed sphere shows the approximate position of the target)

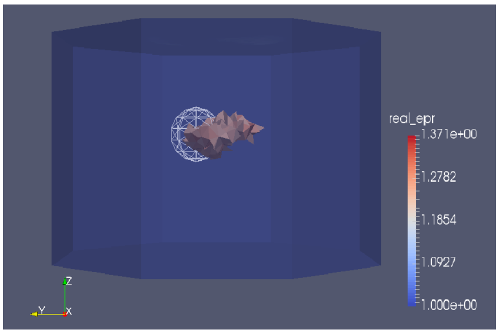

(a) No FPEs (side view)

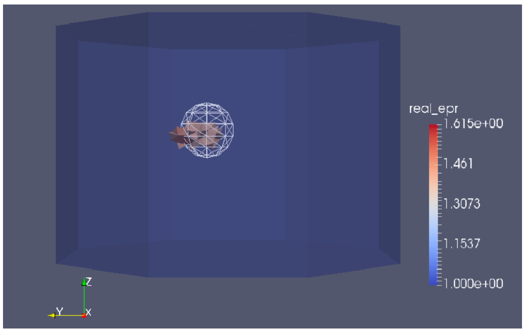

(b) 3 FPE combinations (side view)

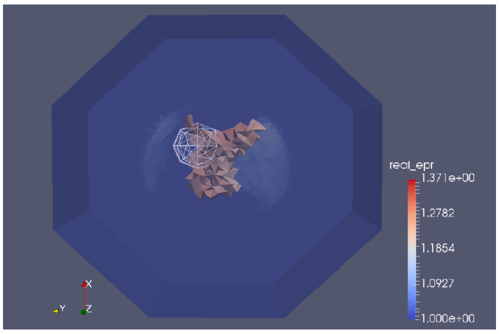

(c) No FPEs (top view)

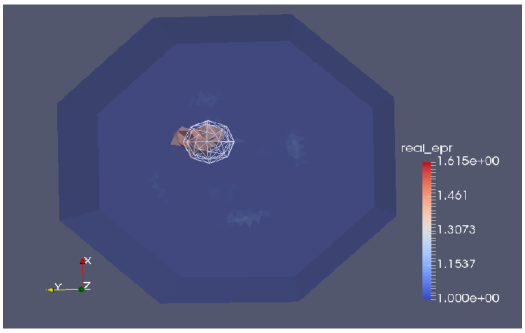

(d) 3 FPE combinations (top view)

Figure 45: Experimental inversion results at 1.15GHz for the target at Position 2. (a,c) are the case where no FPEs are incorporated whereas (b,d) are the case where 3 FPE combinations are utilized. Threshold set from 16.5% below the maximum to the maximum permittivity. (dashed sphere shows the approximate position of the target)

The main objective of this chapter was to show, using experimental inversion results, that utilization of field perturbing elements in a metallic resonant enclosure will lead to increasing the amount of non-redundant data which ultimately leads to better permittivity map reconstructions at the systematically chosen frequency points. It is clearly visible from the results presented herein, that incorporation of field perturbing elements in the chamber enhances the overall imaging performance by eliminating the false positives (artifacts) and help in more accurate reconstruction of the permittiviy map of the OI [2]. Moreover, modelling errors as well as data calibration technique were also discussed and analyzed.

As pointed out earlier, MWI with a metallic enclosure is highly frequency dependent and this frequency dependency is observable in the figures. It is observed that the inversion at 1.13GHz yields slightly more accurate reconstructions compared with those at 1.15GHz.

[2]It is noted that in Fig. 43a and 43c, when no FPEs are utilized the FEM-CSI code is not truly reconstructing because the values of the reconstructed permittivity map of the tetrahedral elements are much lower than the case with FPEs

Chapter 6

Conclusion and Future Work

The goal of the research that was reported herein was to explore alternative ways of enhancing the final image produced in a MWI. Research in the wavefield imaging community has clearly concluded that in any object imaging setting, be it microwave, ultrasound or otherwise, the higher the amount of collected independent data the better and more accurate the reconstructed image of the object of interest will be. Different ways of achieving this goal were discussed in Chapter 2 of this thesis including increasing the spatial sampling points by adding to the number of transmitter/receiver pairs, possibly using the modulated scattering technique, or by varying the boundaries of the imaging chamber, e.g., using a rotational chamber to create unique boundaries per each round of data collection cycle. All such techniques will increase the modelling complexity and/or to the experimental design of the imaging system. The technique proposed and evaluated in this work is to increase the amount of non-redundant data by utilizing reconfigurable field perturbing elements (FPEs) that can be set to active/ON or passive/OFF mode using a probe driver device. This effectively varies the illuminating field without the need for mechanical or rotational change in the boundaries. The FPE technique generates an increased amount of independent data that are collected using a fixed, small, number of transmitter/receiver pairs.

A crucial aspect in design and setup of a MWI system is the design and implementation of the imaging chamber which plays a significant role in obtaining accurate object reconstructions. During this work, we utilized a metallic chamber with flat surfaces in the shape of an octagon which can be considered superior to the quasi-transparent dielectric chambers that are commonly used (typically filled with a lossy immersion medium to reduce modelling error). Some of these advantages are summarized as:

- Octagonal chamber with flat surfaces is easier to model compared with cylindrical or multi-faceted chambers
- Metallic walls allow better control and modelling of unwanted reflections and/or mutual couplings
- the metallic boundaries shield the measurement taken within the chamber from outside noise
- the quasi-resonant nature of such chambers can lead to higher signal-to-noise ratios
- Cavity modes can be easily perturbed using shorting elements such as the FPEs described herein, thus leading to large variations in the illuminating fields

To validate the concept and verify the operation of the field perturbing elements, it was shown, by placing the FPE in an empty chamber with two transmitters, that toggling the mode of the FPEs within the chamber will effectively change the fields inside. Simulated inversion results were presented and examined to confirm that the concept is in fact effective. Subsequently, a complete experimental system was set up to collect and invert measured data from a dry wooden OI placed in two different positions in the chamber. The procedure to select data collection and inversion frequencies as well as the calibration technique were also discussed and the results presented in Chapter 5.

To build upon this work, one can zero in on the design of the reconfigurable plates to be able to design PCB plates that match more closely with the modelled plates. The plates used in this research have been shown to be effective and have good match with the model in certain frequencies. FPEs that have higher accuracy in modelling, would certainly give one the ability to collect data at a higher number of frequency points. Progressive subsequent research should be performed to reduce the modelling error, although one can only get closer to the model but never to match it.

There would be value in studying the dominant polarizations, for each transmitting antenna, within the chamber and customizing FPEs that optimize the perturbation of such modes. For instance when using thin wire monopoles placed normal to the side walls, the dominant component of the electric field inside the chamber is E_ρ and the component with smallest magnitude level is E_z. It is possible to enhance these weak field components by making use of the FPEs. That is, if a dynamic boundary element has a bent L-shape with a prominent size in a desired direction (in this case $\hat{z}$) can help elevate the field intensity for that particular polarization by offering a path for currents along that direction [54].

The research reported in this thesis paves the way for further study on design and implementation of low cost biomedical imaging systems by keeping the design and modelling complexity to a minimum through the use of alternative methods to increase the amount of independent data collected in a MWI system.

References

[1] William Weedon, W.C. Chew, and P. Mayes. "A Step-Frequency Radar Imaging System for Microwave Nondestructive Evaluation". In: *Journal of Electromagnetic Waves and Applications* 14 (Jan. 2000), pp. 665–667.

[2] M. Pastorino, S. Caorsi, and A. Massa. "A global optimization technique for microwave nondestructive evaluation". In: *IEEE Transactions on Instrumentation and Measurement* 51.4 (2002), pp. 666–673.

[3] Lin-Ping Song, Chun Yu, and Qing Huo Liu. "Through-wall imaging (TWI) by radar: 2-D tomographic results and analyses". In: *IEEE Transactions on Geoscience and Remote Sensing* 43.12 (2005), pp. 2793–2798.

[4] Nikolay I. Tulenkov and Vladimir I. Veremyev. "Development of ground penetrating radar system". In: *2018 IEEE Conference of Russian Young Researchers in Electrical and Electronic Engineering (EIConRus)*. 2018, pp. 247–249.

[5] Lorenzo Crocco and Vincenzo Ferrara. "A review on ground penetrating radar technology for the detection of buried or trapped victims". In: *2014 International Conference on Collaboration Technologies and Systems (CTS)*. 2014, pp. 535–540.

[6] Aria Abubakar, Tarek Habashy, Vladimir Druskin, Leonid Knizhnerman, and D. Alumbaugh. "2.5 D forward and inverse modeling for interpreting low-frequency electromagnetic measurements". In: *Geophysics* 73 (July 2008), F165–F177.

[7] Aria Abubakar and Peter Berg. "Non-linear three-dimensional inversion of cross-well electrical measurements". In: *Geophysical Prospecting* 48 (Dec. 2001), pp. 109–134.

[8] Mohammad Asefi, Colin Gilmore, Ian Jeffrey, Joe LoVetri, and Jitendra Paliwal. "Detection and continuous monitoring of localised high-moisture regions in a full-scale grain storage bin using electromagnetic imaging". In: *Biosystems Engineering* 163 (Sept. 2017), pp. 37–49.

[9] Mohammad Asefi, Ian Jeffrey, Joe LoVetri, Colin Gilmore, Paul Card, and Jitendra Paliwal. “Grain Bin Monitoring via Electromagnetic Imaging”. In: 119.C (2015). ISSN: 0168-1699.

[10] Ian Jeffrey, Joe LoVetri, Amer Zakaria, Majid Ostadrahimi, Mohammad Asefi, Colin Gilmore, Paul Card, and Jitendra Paliwal. “Grain bin storage monitoring via microwave imaging”. In: *2013 USNC-URSI Radio Science Meeting (Joint with AP-S Symposium)*. 2013, pp. 209–209.

[11] Mariya Lazebnik, Dijana Popovic, Leah McCartney, Cynthia Watkins, Mary Lindstrom, Josephine Harter, Sarah Sewall, Travis Ogilvie, Anthony Magliocco, Tara Breslin, Walley Temple, Daphne Mew, John Booske, Michal Okoniewski, and Susan Hagness. “A large-scale study of the ultrawideband microwave dielectric properties of normal, benign and malignant breast tissues obtained from cancer surgeries”. In: *Physics in medicine and biology* 52 (Nov. 2007), pp. 6093–115.

[12] Steven Poplack, Tor Tosteson, Wendy Wells, Brian Pogue, Paul Meaney, Alexander Hartov, Christine Kogel, Sandra Soho, Jennifer Gibson, and Keith Paulsen. “Electromagnetic Breast Imaging: Results of a Pilot Study in Women with Abnormal Mammograms 1”. In: *Radiology* 243 (May 2007), pp. 350–9.

[13] Mohammad Asefi, Anastasia Baran, and Joe LoVetri. “An Experimental Phantom Study for Air-Based Quasi-Resonant Microwave Breast Imaging”. In: *IEEE Transactions on Microwave Theory and Techniques* (Apr. 2019).

[14] E. C. Fear, J. Bourqui, C. Curtis, D. Mew, B. Docktor, and C. Romano. “Microwave Breast Imaging With a Monostatic Radar-Based System: A Study of Application to Patients”. In: *IEEE Transactions on Microwave Theory and Techniques* 61.5 (2013), pp. 2119–2128.

[15] Serguei Semenov. “Microwave tomography: Review of the progress towards clinical applications”. In: *Philosophical transactions. Series A, Mathematical, physical, and engineering sciences* 367 (Sept. 2009), pp. 3021–42.

[16] Ria Benny, Thathamkulam Anjit, and Palayyan Mythili. “An overview of microwave imaging for breast tumor detection”. In: *Progress In Electromagnetics Research B* 87 (Jan. 2020), pp. 61–91.

[17] Sollip Kwon and Seungjun Lee. “Recent Advances in Microwave Imaging for Breast Cancer Detection”. In: *International Journal of Biomedical Imaging* 2016 (Jan. 2016), pp. 1–25.

[18] Anastasia Baran, Amer Zakaria, Douglas Kurrant, Elise Fear, and Joe LoVetri. “Breast Imaging Using Microwave Tomography with Radar-Based Tissue-Regions Estimation”. In: *Progress In Electromagnetics Research* 149 (2014), pp. 161–171.

[19] Mohammad Asefi, Majid OstadRahimi, Amer Zakaria, and Joe LoVetri. “A 3-D Dual-Polarized Near-Field Microwave Imaging System”. In: *IEEE Transactions on Microwave Theory and Techniques* 62.8 (2014), pp. 1790–1797.

[20] Amer Zakaria, Colin Gilmore, and Joe LoVetri. “Finite-element contrast source inversion method for microwave imaging”. In: *Inverse Problems* 26 (Nov. 2010), pp. 115010–21.

[21] EIL. *Electromagnetic Imaging Labratory*. URL: `https://home.cc.umanitoba.ca/~lovetrij/EMILab/`. (University of Manitoba).

[22] Pedram Mojabi and Joe LoVetri. “Experimental Evaluation of Composite Tissue-Type Ultrasound and Microwave Imaging”. In: *IEEE Journal on Multiscale and Multiphysics Computational Techniques* 4 (2019), pp. 119–132.

[23] V. Khoshdel, Mohammad Asefi, Ahmed Ashraf, and Joe LoVetri. “Full 3D Microwave Breast Imaging Using a Deep-Learning Technique”. In: *Journal of Imaging* 6 (Aug. 2020), p. 80.

[24] Joe LoVetri, Mohammad Asefi, Colin Gilmore, and Ian Jeffrey. “Innovations in Electromagnetic Imaging Technology: The Stored-Grain-Monitoring Case”. In: *IEEE Antennas and Propagation Magazine* 62.5 (2020), pp. 33–42.

[25] Max Hughson. *Quantitative Transmission Tomography for Non-Destructive Imaging of Stored Grain and Biological Tissue*. University of Manitoba, 2021.

[26] Colin Gilmore, Mohammad Asefi, Kyle Nemez, Jitendra Paliwal, and Joe LoVetri. "Three dimensional radio-frequency electromagnetic imaging of an in-bin grain conditioning process". In: *Computers and Electronics in Agriculture* 167 (Nov. 2019), p. 105059.

[27] Majid Ostadrahimi, Amer Zakaria, Joe LoVetri, and Lotfollah Shafai. "A Near-field Dual Polarized (TE-TM) Microwave Imaging System". In: *IEEE Transactions on Microwave Theory and Techniques* 61 (Mar. 2013).

[28] Kyle Nemez, Mohammad Asefi, Anastasia Baran, and Joe LoVetri. "A faceted magnetic field probe resonant chamber for 3D breast MWI: A synthetic study". In: July 2016, pp. 1–3.

[29] Puyan Mojabi and Joe LoVetri. "Microwave Biomedical Imaging Using the Multiplicative Regularized Gauss–Newton Inversion". In: *Antennas and Wireless Propagation Letters, IEEE* 8 (Feb. 2009), pp. 645–648.

[30] Amer Zakaria, Ian Jeffrey, and Joe LoVetri. "Full-Vectorial Parallel Finite-Element Contrast Source Inversion Method". In: *Progress In Electromagnetics Research* 142 (Jan. 2013), pp. 463–483.

[31] Kevin Brown, Nicholas Geddert, Mohammad Asefi, Joe LoVetri, and Ian Jeffrey. "Hybridizable Discontinuous Galerkin Method Contrast Source Inversion of 2-D and 3-D Dielectric and Magnetic Targets". In: *IEEE Transactions on Microwave Theory and Techniques* 67 (May 2019), pp. 1766–1777.

[32] Elaheh Gorgin. *An Analysis Of Multiplicative Regularization.* PhD thesis, Michigan Technological University, 2015.

[33] Pedram Mojabi and Joe LoVetri. "Ultrasound tomography for simultaneous reconstruction of acoustic density, attenuation, and compressibility profiles". In: *The Journal of the Acoustical Society of America* 137.4 (2015), pp. 1813–1825.

[34] Kyle Nemez, Anastasia Baran, Mohammad Asefi, and Joe LoVetri. "Modeling Error and Calibration Techniques for a Faceted Metallic Chamber for Magnetic Field Microwave Imaging". In: *IEEE Transactions on Microwave Theory and Techniques* 65.11 (2017), pp. 4347–4356.

[35] Mohammad Asefi, Gabriel Faucher, and Joe LoVetri. "Surface-Current Measurements as Data for Electromagnetic Imaging Within Metallic Enclosures". In: *IEEE Transactions on Microwave Theory and Techniques* 64.11 (2016), pp. 4039–4047.

[36] Puyan Mojabi and Joe LoVetri. "A Novel Microwave Tomography System Using a Rotatable Conductive Enclosure". In: *IEEE Transactions on Antennas and Propagation* 59.5 (2011), pp. 1597–1605.

[37] Mohammad Asefi. *Stored-grain Monitoring Utilizing Radio Wave Imaging*. PhD thesis, University of Manitoba, 2016.

[38] J. Jin. *The Finite Element Method in Electromagnetics*. John Wiley Sons, Inc, 2002.

[39] Mohammad Asefi and Joe LoVetri. "Use of Field-Perturbing Elements to Increase Nonredundant Data for Microwave Imaging Systems". In: *IEEE Transactions on Microwave Theory and Techniques* 65.9 (2017), pp. 3172–3179.

[40] Peter M van den Berg and Ralph E Kleinman. "Comparison of an Enhanced Distorted Born Iterative Method and the Multiplicative-Regularized Contrast Source Inversion method". In: *Inverse Problems* 13.6 (1997), p. 1607.

[41] Colin Gilmore, Puyan Mojabi, and Joe LoVetri. "Comparison of an Enhanced Distorted Born Iterative Method and the Multiplicative-Regularized Contrast Source Inversion method". In: *Antennas and Propagation, IEEE Transactions on* 57 (Sept. 2009), pp. 2341–2351.

[42] Amer Zakaria and Joe LoVetri. "Application of Multiplicative Regularization to the Finite-Element Contrast Source Inversion Method". In: *IEEE Transactions on Antennas and Propagation* 59.9 (2011), pp. 3495–3498.

[43] O. M. Bucci and T. Isernia. "Electromagnetic inverse scattering: Retrievable information and measurement strategies". In: *Radio Science* 32.6 (1997), pp. 2123–2137.

[44] Martina Teresa Bevacqua and Tommaso Isernia. "Quantitative Non-Linear Inverse Scattering: A Wealth of Possibilities Through Smart Rewritings of the Basic Equations". In: *IEEE Open Journal of Antennas and Propagation* 2 (2021), pp. 335–348.

[45] Colin Gilmore and Joe LoVetri. "Enhancement of microwave tomography through the use of electrically conducting enclosures". In: *Inverse Problems* 24 (June 2008).

[46] J. Bolomey and F. Gardiol. *Engineering applications of the modulated scatterer technique*. Artech House Publishers, 2001.

[47] Ovidio Mario Bucci, Lorenzo Crocco, and Rosa Scapaticci. "On the Optimal Measurement Configuration for Magnetic Nanoparticles-Enhanced Breast Cancer Microwave Imaging". In: *IEEE Transactions on Biomedical Engineering* 62.2 (2015), pp. 407–414.

[48] Sasaki Kensuke, Wake Kanako, and Soichi Watanabe. "Development of best fit Cole-Cole parameters for measurement data from biological tissues and organs between 1 MHz and 20 GHz". In: *Radio Science* 49 (June 2014), pp. 459–472.

[49] Agilent Technologies. *Technical Overview, 85070E Dielectric Probe Kit 200 MHz to 50 GHz*. URL: https://82fai3h5wg8220a0l3ilfiz1-wpengine.netdna-ssl.com/wp-content/uploads//2015/09/HP_85070E.pdf/. Agilent Technologies, Inc. 2003, 2005.

[50] Edward C Jordan. *Electromagnetic waves and radiating systems*. Prentice-Hall, 1968.

[51] GrainViz. *151 Research Inc.* URL: https://www.grainsystems.com/en_US/products/grain-management.html/. (grainsystems).

[52] Matthew J. Burfeindt, Nader Behdad, Barry D. Van Veen, and Susan C. Hagness. "Quantitative Microwave Imaging of Realistic Numerical Breast Phantoms Using an Enclosed Array of Multiband, Miniaturized Patch Antennas". In: *IEEE Antennas and Wireless Propagation Letters* 11 (2012), pp. 1626–1629.

[53] Majid Ostadrahimi, Puyan Mojabi, Colin Gilmore, Amer Zakaria, Sima Noghanian, Stephen Pistorius, and Joe LoVetri. "Analysis of Incident Field Modeling and Incident/Scattered Field Calibration Techniques in Microwave Tomography". In: *Antennas and Wireless Propagation Letters, IEEE* 10 (Feb. 2011), pp. 900–903.

[54] R. Garg. *Coaxial Line Discontinuities.* John Wiley Sons, Inc, 2005.